Collagenesis Orchestrates Mechanoadaptive Homeostasis of Intervertebral Disc.

Authors

Jian He[1, 8,*], Sha Huang[1,8], Yangyang Li[1], Yingbo Wang[1], Pulin Yan[1], Ou Hu[1], Peng Lin[1], Huaijian Jin[1], Jun Zhu[1], Liang Zhang[1], Yaoyao Liu[1], Qin Qin[2], Yu Guo[3], Xiuhui Zheng[4], Yangli Xie[5], Lin Chen[5], Yu Lan[6], Bing Liu[7,*], Peng Liu[1,*] , Yibo Gan[1,*]

Affiliations

[1] Department of Spine Surgery, Center of Orthopedics, State Key Laboratory of Trauma and Chemical Poisoning, Daping Hospital, Army Medical University, Chongqing 400042, China;

[2] Department of Painology, Daping Hospital, Army Medical University, Chongqing 400042, China;

[3] Department of Radiology, Daping Hospital, Army Medical University, Chongqing 400042, China;

[4] Department of Gynecology and Obstetrics, Daping Hospital, Army Military Medical University, Chongqing 400042, China

[5] Center of Bone Metabolism and Repair, State Key Laboratory of Trauma, Burns and Combined Injury, Trauma Center, Research Institute of Surgery, Laboratory for the Prevention and Rehabilitation of Military Training Related Injuries, Daping Hospital, Army Medical University, Chongqing 400042, China;

[6] State Key Laboratory of Experimental Hematology, Haihe Laboratory of Cell Ecosystem, Key Laboratory for Regenerative Medicine of Ministry of Education, Institute of Hematology, School of Medicine, Jinan University, Guangzhou 510632, China;

[7] State Key Laboratory of Experimental Hematology, Haihe Laboratory of Cell Ecosystem, Senior Department of Hematology, the Fifth Medical Center, Medical Innovation Research Department, Chinese PLA General Hospital, Beijing 100071, China;

[8] These authors contributed equally: Jian He and Sha Huang

* Correspondence: jianhe.amms@gmail.com (J.H.); bingliu17@yahoo.com (B.L.); liupengd@tmmu.edu.cn (P.Liu); ganyibo@tmmu.edu.cn (Y.G.)

Abstract

Intervertebral discs are crucial to spine flexibility and stability during locomotion, but the mechanism of their mechanoadaptation to stress remains inadequately elucidated. We discovered spontaneous collagenesis in discs at the tail base in mice occurring from 14 days post-natal development. These discs termed as type C, differ from typical discs by exhibiting intensive collagen II and reduced aggrecan deposition contributing to the stiffening of the extracellular matrix (ECM), without typical degenerative markers. The reinforced mechanical properties enable type C discs to withstand high mechanical stress during flexion. Further analysis revealed that type C discs experience a turnover in cell composition, with the emergence of Procr^{+} progenitor cells and depletion of notochord cells. We demonstrated the essential role of mechanical stress in type C disc formation, suggesting a mechanoadaptive process rather than a pathological condition. Mechanistically, we identified TRPV4, as pivotal factors in collagen II synthesis in type C discs, highlighting the role of mechanotransduction in this adaptation. Our findings introduce a novel mechanoadaptive process of intervertebral disc by orchestrating collagenesis, advancing understanding of diverse disc functions in spine development and homeostasis, thereby providing insights for leveraging this mechanism to address spinal disorders.

Introduction

The spine is the central skeletal scaffolding for the body, providing support for locomotion and protecting the spinal cord and nerves. The intervertebral disc (IVD) is the critical unit responsible for bearing mechanical stress to maintain spinal integrity. It is commonly believed that mechanical overload can lead to IVD degeneration (1, 2). Cross-sectional population studies show that degenerative changes in IVD can occur in various percentages of individuals, ranging from 12% in those under 18 years old to 70% in those under 50 years old (3–6). However, more than 95% of these individuals are either asymptomatic or have received a diagnosis for disease condition (7, 8). These discrepancies indicate that the IVD is able to withstand the physical demands of daily activities in most cases, prompting further investigation into the mechanisms that allow the spine to adapt to mechanical stress.

The mouse spine disc shows substantial similarities in aspects of geometry and mechanical properties to those of humans, ensuring its potential in studying the mechanism of human disc

adapted to mechanical stress (9, 10). The mouse tail is experiencing sudden tilt perturbations, serving as "dynamic rudder" in body balance (11). Despite the significant and continuous mechanical stress from these demands, it is commonly believed that the mouse disc is able to maintain its homeostasis until old age (12, 13). This raises a scientific question about the fundamental cellular and molecular basis underlying this mechanical adaptation.

Here, we revealed a heretofore unrecognized type of disc featured by spontaneous collagenesis (termed as type C) by constructing spatiotemporal profiles of the mouse spine across the postnatal development. In contrast with the typical one fulfilled with proteoglycan and notochord cells (NCs), type C discs are located at the base of mouse coccygeal spine featured by reduced aggrecan deposition but intensive collagen II content, and a lack of typical degenerative markers. The consequent ECM stiffening leads to reinforced mechanical properties. Single-cell RNA-sequencing analysis revealed that type C discs enriched $Procr^{+}$ progenitor cells as we identified in previous studies (14, 15), showing NC-independent developmental origins. The examination on coccygeal spine after unloading demonstrated the essential role of mechanical stress in formation of type C discs. We further characterized the mechanosensory genes, particularly TRPV4, that regulate the collagen II synthesis in type C discs. These findings provide critical insights into the mechanoadaptive mechanisms of IVDs that are essential for preserving disc homeostasis, which are crucial for devising strategies to improve spinal function and potentially alleviate relevant disorders.

Results

Spatial-temporal profiling of the mouse spine delineates the unparalleled development of coccygeal discs in the tail base.

To investigate the impact of mechanical stress on the postnatal development of the spine, Micro-CT imaging was utilized to examine the structural differences in vertebrae of one-month-old mice (Supplementary Figure 1A). The results indicated that vertebrae ranging from the second coccygeal vertebra (Co2) to Co8 exhibited an hourglass shape, increased bone volume and moment of inertia, suggesting their enhanced strength in resisting mechanical loads (Supplementary Figure 1, B and C)(16, 17). Furthermore, we found a reduced relative disc height index and disc convexity index in these segments (Supplementary Figure 1D). Considering the involvement of coccygeal segments in

tail movements in mice, it is reasonable to hypothesize that this spine segment experiences intense mechanical stress(18, 19).

We then profiled the histological characteristics of spine segments spanning from Co2 to Co8 during postnatal development (Figure 1A). We identified substantial variations in disc morphology at postnatal day 7 (P7) and beyond (Figure 1B). Notably, Co4/5 and Co5/6 showed lower disc heights after P28 (Figure 1C and Supplementary Figure 1E). We observed significantly higher histological scores in Co4/5 and Co5/6 discs from P28 to 12 months (Figure 1D), primarily contributed by changes in features of the NP and annulus fibrosus (AF) (Supplementary Figure 1F)(20). Subsequently, Thompson grading (21, 22) revealed that a higher proportion of NP and AF in Co3/4, Co4/5 and Co5/6 were categorized as grade 3 during postnatal development, indicating a dramatic structural change in these discs (Figure 1E). We then used T2-weighted magnetic resonance imaging (MRI) to examine the radiological features. The results showed notable reductions in MRI index and T2 relaxation time at the Co3/4, Co4/5 and Co5/6 levels compared to Co2/3, Co6/7, and Co7/8, indicating decreased hydration in these discs (Figure 1F and Supplementary Figure 1G). To sum up, the comprehensive histological profile of the mouse spine revealed distinct morphological features in Co3/4, Co4/5, and Co5/6, displaying lower disc heights and higher histological scores, suggesting a unique developmental program for these discs.

Characterization of collagen-abundant discs in the mouse tail spine

Next, we analyzed the macroscopic characteristics of Co3/4, Co4/5 and Co5/6 discs. Strikingly, these discs exhibited a non-gelatinous NP and indistinct borderlines between the NP and AF (Figure 2A). In contrast, the Co2/3, Co6/7 and Co7/8 discs demonstrated a typical appearance characterized by a well-defined NP filled with water content (Figure 2A). Morphological changes were evident in the Co4/5 disc, as indicated by the loss of NP/AF demarcation, reduced NP cell count, and presence of clefts (Figure 2B). Polarized light imaging revealed a higher deposition of collagen fiber in the NP of Co4/5 disc, which was absent in the NP of Co7/8 disc (Figure 2, C and D). Spatiotemporally, this collagen accumulation occurred in Co4/5 and Co5/6 discs since postnatal day 14 (Supplementary Figure 2, A and B). Quantitative analysis demonstrated a similar composition of collagen fibers in the AF of both discs (Figure 2E and Supplementary Figure 2C), suggesting that structural alterations and collagen fiber accumulation primarily occurred in NP.

To determine the differences in ECM composition, we used FTIR spectroscopy to assess the protein context in Co7/8 and Co4/5 discs. The results revealed significantly higher collagen synthesis in NP and AF of Co4/5 disc (Figure 2F). Concurrently, we observed proteoglycan degradation alongside an increase in collagen and total protein content in NP of Co4/5 disc (Figure 2, G and H). A minor elevation in collagen content was noted in the endplate (EP) of Co4/5 disc (Supplementary Figure 2, D and E). The differences in NP and AF could be detected as early as P14 (Supplementary Figure 2F). Our findings confirmed the prevalence of collagen deposition in the Co3/4, Co4/5 and Co5/6 discs. These distinct variances in the ECM led to the hypothesis of a novel disc type in the coccygeal spine, designated as collagenic disc (type C), in contrast to the typical aggrecan-enriched disc morphology (type A). The prevalence rates of type C discs range from 45.7% to 82.9% at Co3/4, Co4/5, and Co5/6 levels (Figure 2I). Therefore, our findings illustrate the presence of two distinct types of discs in the mouse tail, each exhibiting unique characteristics that imply diverse functions within the spine (Figure 2J).

Type C disc presents an ECM remodeling instead of degenerative consequences

We then conducted RNA-seq to compare the transcriptomic differences between type A and type C discs. PCA clearly distinguished the two types of discs, revealing 255 significantly differentially expressed genes (DEGs) for type C and 424 DEGs for type A discs (Figure 3, A and B, and Supplementary Table 1). Strikingly, the core matrisome term with collagens was found to be significantly enriched in the signature genes of type C discs (Figure 3C). Specifically, *Col2a1* but not *Col1a1*, is highly expressed in type C discs, while *Acan*, encoding a proteoglycan, is highly expressed in type A discs (Figure 3D). Immunostaining analysis confirmed the collagen II deposition and aggrecan degradation particularly in the NP of type C discs (Figure 3E). Additionally, signature genes of NCs such as *T*, *Krt8*, *Krt18*, and *CD24a* (23, 24), were significantly downregulated in type C discs compared to type A discs (Figure 3F). Functional enrichment analysis revealed that the upregulated DEGs in type A discs were associated with cell adhesion and notochord morphogenesis, whereas those in type C discs were linked to cellular calcium ion homeostasis, and cell chemotaxis (Supplementary Figure 3, A and B). Gene set variation analysis (GSVA) confirmed that type C discs displayed a higher level of chondrocyte differentiation and a lower level of oxidative phosphorylation (Figure 3G). Interestingly, Weighted Gene Co-Expression Network

Analysis (WGCNA) identified a module correlated with mechanosensation (*Piezo1* and *Trpv4*) in type C discs (Supplementary Figure 3, C to E).

To exclude the possibility of early onset of degeneration in type C discs, we conducted a comparative analysis of key markers associated with IDD (25). Our results revealed that levels of IL-1β, a pro-inflammatory cytokine, were expressed at a lower level in NP and elevated in the AF of type C discs (Figure 3, H and I). The expression level of MMP3, a matrix metalloproteinase involved in ECM degradation, was even lower in NP of type C discs (Figure 3, H and I). Notably, typical degenerative characteristics observed in other mouse models were not evident in type C discs (Supplementary Figure 3F) (26–29). Furthermore, IDD-related genes in ECM homeostasis, autophagy, apoptosis and oxidative stress did not exhibit distinct patterns between type A and type C discs (Supplementary Figure 3G). In addition, the heightened expression of *Bcl2* while *Bax* remains unchanged in type C discs indicates an anti-apoptotic response in type C discs (Figure 3J). Collectively, our results highlight ECM remodeling from aggrecan to collagen II in NP of type C discs without manifesting typical degenerative characteristics.

Type C disc exhibits superior mechanical properties in response to stress

To evaluate the mechanical properties of these two types of discs, we used atomic force microscopy (AFM) to probe the surface characteristics and mechanical response by applying a controlled force (Figure 4A). Our analysis indicated higher viscoelasticity in NP, which was characterized by a tortuous force-displacement curve (Figure 4B). The increased hysteresis during the approaching-retraction cycle reflected enhanced stiffness in type C discs, suggesting a more robust and resilient mechanical structure (Figure 4, B and C).

In order to assess the elastic properties under extreme stress, we conducted compression and three-point bending tests on functional spine units (FSUs) with two types of discs (Figure 4D). The compression test revealed significantly higher maximum stress and linear region modulus in FSUs with type C disc, indicating their greater resistance to elastic deformation compared to type A discs (Figure 4, E and F). Interestingly, the lower strains at both the transition and maximum points in FSUs with type C disc suggested their restricted flexibility (Figure 4G). Three-point bending tests showed that double FSUs (dFSUs) with two type C discs exhibited higher bending strength and linear region modulus compared to those with two type A discs (Figure 4, H to J). To capture

177 mechanical dynamics during reciprocating locomotion, we then conducted cyclic axial tension-
178 compression test (Figure 4K). FSUs with type C discs showed a notably reduced length of neutral
179 zone (NZ) in the tensile curve and axis range of motion in both compressive and tensile curves,
180 aligning with their decreased disc height and limited flexibility as observed in previous analysis
181 (Figure 4L). The higher NZ stiffness in FSUs with type C discs, when compared to that with type
182 A discs, suggests the capacity to withstand higher stress (Figure 4L). Notably, the anticipated rise
183 in compressive stiffness, often associated with disc degeneration(22), was absent in type C discs
184 (Figure 4L). Taken together, these results suggest that type C discs possess enhanced mechanical
185 properties to endure mechanical stress, albeit at the cost of flexibility, providing a physiological
186 basis for adapting to demanding mechanical conditions.
187
188 **scRNA-seq analysis reveals the cellular alterations and distinct developmental origin of type**
189 **C disc**
190 We performed single cell RNA-seq (scRNA-seq) analysis to investigate the cellular heterogeneity
191 of two distinct types of discs (Supplementary Figure 4A). Integrated analysis revealed nine cell
192 clusters based on the expression of canonical marker genes, encompassing NCs (cluster 1), four
193 subsets of chondrocyte (clusters 2-5, RegC, HyperC, FibroC and CycC, representing regulatory,
194 hypertrophic, fibrotic and cycling chondrocytes respectively), osteoprogenitor cells (cluster 6, OP),
195 disc progenitor cells (cluster 7, PC), as well as endothelial and blood cells (clusters 8 and 9) (Figure
196 5, A and B, Supplementary Figure 4B and Table 2). Cell composition analysis revealed an abundance
197 of NCs expressing Brachyury (encoded by *T*) in type A discs, whereas PCs expressing EPCR
198 (encoded by *Procr*) which have been identified in human and goat discs (14, 15), emerged in type
199 C discs (Figure 5, C and D). Furthermore, deconvolution of bulk transcriptomic dataset confirmed
200 the scarcity of NCs in type C discs (Supplementary Figure 4C). Notably, the residual NC in type C
201 disc exhibited elevated expression of collagen-related genes, such as *Col1a2*, *Col2a1*, and *Col3a1*,
202 which enriched processes related to collagen biosynthesis (Figure 5E and Supplementary Figure
203 4D). PCs in type C discs showed increased expression of *Dpp4* and *Thy1*, signature genes associated
204 with stem and progenitor cells (Figure 5E) (30, 31).
205 We then compared the differences in chondrocyte clusters between type A and type C discs. Genes
206 related to chondrocyte differentiation such as *Cnmd*, *C4b*, *Comp*, *Col9a1* and *Cytl1* were found to

be significantly upregulated in type C disc (Figure 5F and Supplementary Figure 4, E to G). Moreover, the expression of *Lepr*, *Car1*, and *Adgrg1*, which are specific to chondrocyte progenitors, was significantly higher in type A disc (Supplementary Figure 4H) (32). Pathway analysis revealed enrichment of chondrogenesis-related pathways including PI3K-Akt, TGF-beta and HIF-1 signaling in type C discs (Figure 5G). These results suggest a more pronounced chondrocyte differentiation in type C discs than that in type A discs. Furthermore, we did not find differences in cell senescence or oxidative stress in the chondrocyte clusters, suggesting independence from degenerative and aging processes in type C discs (Supplementary Figure 4I).

To explore the developmental origins of NCs, PCs and chondrocytes, we reanalyzed disc cell clusters from scRNA-seq on Shh-Cre;tdTomato mice, which enable tracking of NCs and their descendants (Supplementary Figure 5, A and B) (33). We used the signature genes of cell clusters in coccygeal disc in our study to identified the cell clusters in lumbar discs (Figure 5H and Supplementary Figure 5, C and D). NCs highly express the *tdTomato* gene, as expected (Figure 5I). Notably, we observed minimal presence of tdTomato^{+} cells in PCs, osteoblasts, and chondrogenic clusters, suggesting their notochord-independent developmental pathways (Figure 5J).

Overall, our scRNA-seq analysis unveiled heightened chondrogenic differentiation for collagen synthesis in type C discs, marked by an increase in PC population and a corresponding reduction in NC population within the NP, showcasing distinct embryonic origins with type A discs.

Mechanical stress is essential for the formation of type C disc

We postulated that the increased mechanical properties of type C discs are regulated by their elevated mechanical condition. Due to the difficulty in directly measuring mechanical parameters in mouse discs during tail locomotion, we constructed a finite element model (FEM) using Micro-CT images of the lumbo-sacro-coccygeal spine (Figure 6A, Supplementary Figure 6A and Table 3). This method has been widely employed to analyze the mechanical dynamics of tissues under certain conditions (34, 35). By conducting simulations of natural lateroflexion, dorsiflexion and plantarflexion (Supplementary Figure 6B and Video 1 to 3), we identified an escalation in force within the discs ranging from Co2/3 to Co5/6, along with concentrated moments in the Co3/4 to Co5/6 discs (Figure 6, B and C). The assessments on these flexions revealed an elevation in the von Mises stress on the AF and EP of the Co3/4, Co4/5, and Co5/6 discs (Figure 6D and Supplementary

Figure 6, C and D). Principal component analysis of stresses categorized discs from different levels into two clusters, including type A (Co2/3, Co6/7, and Co7/8) and type C (Co3/4, Co4/5, and Co5/6) (Figure 6E), consistent with the findings from histological analysis. Notably, NP of type C discs experienced higher mechanical stress compared to type A discs during flexion (Supplementary Figure 6, E and F).

To investigate the necessity of mechanical stress on the formation of type C discs, we performed microdissection to excise the tendon around the tail base at Co5 on the date of birth (Figure 6F). The growth and development of the mouse were not impeded but the tail length was shortened by the tendon detachment, accompanied by decreases in the heights of vertebrae ranging from Co6 to C8 and discs ranging from C5/6 to Co7/8 (Supplementary Figure 7, A and B). On day 30 post-detachment, mice were subjected to treadmill testing to confirm the success of mechanical unloading of the tail (Supplementary Figure 7C and Video 4). Strikingly, we found a significant decrease in the prevalence of type C disc at Co5/6 and Co6/7, which experienced mechanical unloading postnatally (Figure 6G). Accordingly, histopathological scores of type C discs in tendon detachment were markedly lower compared to the normal control with a sham operation (Figure 6H and Supplementary Figure 7D), indicating that mechanical stress is essential for the formation of type C discs.

TRPV4-mediated mechanoadaptation affects the function of type C disc

The high mechanical stress in type C discs prompted us to inquire about the potential role of mechanical sensing signaling. We observed a significant upregulation of the *Piezo1, Piezo2* and *Trpv4* genes, which are known to be involved in mechanosensitive signaling pathways (36, 37) (Figure 7A and Supplementary Figure 8A). Consistently, a heightened presence of $TPRV4^{+}$ and $PIEZO1^{+}$ cells was predominantly observed in NP of type C discs (Figure 7B), indicating the potential role of mechanosensitive signaling pathways.

To investigate the role of mechanosensitive channel TRPV4 in type C disc, we generated *Trpv4* knockout (*Trpv4*-KO) mice (Supplementary Figure 8B). Compared to their wildtype (WT) littermates, *Trpv4*-KO mice did not exhibit significant differences in general traits, tail length, or disc heights (Supplementary Figure 8, C to E). However, type C discs from *Trpv4*-KO mice showed morphological changes, with obstruction to COL II synthesis in the NP and AF (Figure 7C and

Supplementary Figure 8F). Compression and 3-point bending tests revealed a decreased linear modulus response to compression in the FSUs with type C disc in *Trpv4*-KO mice, while their ability to respond to bending remained unaffected (Figure 7D). These findings confirm the crucial role of Trpv4 in ECM remodeling and resulting enhancement of mechanical properties during type C disc formation.

We administered a TRPV4 agonist GSK1016790A to type A discs on postnatal day 0, in an attempt to trigger type C discs during postnatal development. (Figure 7E). Disc treated with the agonist exhibited significantly increased characteristics of type C with collagen deposition, along with increased histopathological scores, compared to the sham control at day 30 post-administration (Figure 7, F and G). Conversely, injections of a PIEZO1 agonist Yoda1 did not induce features of type C disc (Supplementary Figure 8, G and H). These data further emphasize the importance of TRPV4 activation in ECM remodeling and suggest the potential to produce type C discs. In summary, our findings indicate that mechanical stress promotes the formation of type C discs through Trpv4-mediated mechanotransduction.

Discussion

The intervertebral disc serves as a shock absorber during axial loading, maintaining spinal stability and allowing controlled vertebral movement. By comprehensively profiling the spine in growing mice, we identified a heretofore unidentified disc type (type C) characterized by collagenesis. We consider this to be a mechanoadaptive strategy in response to mechanical stress during spine development. Our findings challenge the traditional view that mechanical stress primarily leads to degeneration or other functional deterioration. This paradigm shift opens up new avenues for deciphering the intricate relationship between mechanoadaptation and its physiological basis, leading to innovative approaches for preventing and treating disc diseases, enhancing spinal stability and overall health.

Mechanical stress resulting from bipedalism is recognized as the primary etiological factor for spinal conditions in humans, notably contributing to the high prevalence of lumbar disc degeneration (1, 2, 38). However, a recent clinical trial study found that engaging in progressive walking can reduce the risk of recurrent low back pain, indicating that the reinforcement by mechanical stress prevents spine dysfunction (39). Our study on mice reveals that type C discs exhibit enhanced mechanical

properties to withstand compression and bending stress. The ECM remodeling with increased collagen II and decreased aggrecan within the NP endows the function of type C discs positioned in the highly mechanically stressed area of the mouse tail base. We excluded the possibility of early onset of degeneration as these discs are occurred as early as postnatal day 7 and of lacking typical degenerative characteristics. In contrast, type A discs are common in areas of the spine with lower mechanical stresses, displaying typical characteristics associated with spinal flexibility. This close cooperation is integral for maintaining disc homeostasis while preventing disc from excessive stress (Figure 8). The collagenesis observed in mouse discs may reflect a mechanoadaptive mechanism observed in young human discs (40), which do not result in pathological outcomes under the mechanical loads of daily activities (41). Augmenting collagen deposition, potentially through fibroblast transplantation, could further stabilize the mechanical properties in spine (42), suggesting the mechanical regulation of disc by targeting ECM.

The rodent disc is considered to comprise high retention of NCs that expressing Brachyury (encoded by *T*) in discs throughout their lifespan (9, 43). Nonetheless, our study revealed a distinct disc phenotypes of type C displaying a depletion in NCs. Recent research suggests that the scarcity of T expression is a determining factor in human evolution of tail loss (44), aligning with our concept that the absence of T^+ NCs in type C discs further represents a mechanoadaptive adaptation in mouse spines. Interestingly, we discovered that type C discs enrich $Procr^+$ progenitor cells, a population also identified in healthy human and goat IVDs (14, 15). Our analysis revealed $Procr^+$ progenitor cells have a notochord-independent origin, suggesting the distinct developmental paths between type C and type A discs.

To elucidate the underlying mechanism, we established a mouse model with tendon detachment to achieve stress unloading. The reduced frequency and collagenesis in type C discs validate that mechanical stress is essential for the formation of type C discs. Our findings revealed the effectiveness of Pros and Cons of mechanical stress in maintaining disc function, indicating that a delicate balance of forces is crucial for optimal disc health. Given that the mechanical load on the disc varies during mouse tail locomotion (45, 46), further research is needed to quantify the loads associated with different locomotion scenarios, in order to better understand the balance between the "safe window" and "wear and tear" theories (47). Exploring how different mechanical environments impact disc cellular behavior is essential to pinpoint potential therapeutic approaches

for enhancing disc resilience and preventing degeneration. This involves studying the molecular pathways activated by mechanical loading and unloading, as well as understanding the role of various cell types in responding to these mechanical changes.

Our transcriptomic analysis suggests that mechanosensation plays a significant role in shaping type C discs. This is evidenced by disruptions in collagen II synthesis observed following knockout of the mechanosensitive gene *Trpv4*. The crucial roles of TRPV4 in regulating IVD mechano-biology have been confirmed (48, 49), with studies showing that inhibiting Trpv4 can prevent IVD degeneration (50–53). Recent research demonstrated that Trpv4 knockout resulted in increased *Acan* mRNA expression, elevated PRG4 protein levels, and reduced histological scores in Co6/7 discs of 4 and 8-month-old mice (54). This effect is consistent with our finding that Trpv4-KO led to the prevention of type C disc characteristics. The roles of TRPV4 in murine discs are diverse, exerting positive effects in developing and healthy discs but exacerbating degeneration in diseased discs(55). This distinction is crucial when devising intervention strategies (56–58). Our study suggests that exogenous activation of TRPV4 by its agonist GSK101 holds promise in promoting the formation of new type C disc, thereby warranting further investigation into its targeting strategy to promote disc homeostasis and prevent spinal disorders.

Materials and Methods

Mouse strains

The animal procedures conducted in this study were ethically reviewed and approved by the Animal Ethics Committee of the Third Military Medical University (AMUWEC20223385). C57BL/6J mice were sourced from the Experimental Animal Centers of the Third Military Medical University, SPF (Beijing) Biotechnology Co., Ltd, and Vital River Laboratory Animal Technology Co., Ltd (China). Housing and breeding of the mice took place in a regulated specific pathogen-free (SPF) facility at Daping Hospital, Chongqing, China, under controlled temperature, humidity, and lighting conditions. Trpv4 knockout mice were generated utilizing a CRISPR/Cas9/gRNA targeting strategy to delete exons 3, 4, and 5 of the Trpv4 gene allele (Cyagen, China). Heterozygous parents were mated to generate Trpv4 knockout and wild-type (WT) littermates. The F1 generation was validated by PCR using specific primer pairs: 5'-GGAATGATGGTGATTTTGGCTAAC-3' and 5'-GGTGGCTATTTAGGGACATGGC-3' for Trpv4 knockout mice, and 5'-

CTACTTTGGTGAGTAGCGGTGGAG-3' along with 5'-GGTGGCTATTTAGGGACATGGC-3' for Trpv4 wild-type mice, yielding PCR products that differed in size by 56 base pairs for WT (499 bp) and knockout (555 bp) mice (Supplementary Figure 8B).

MRI scanning

Forty-seven one-month-old mice were euthanized by receiving an intraperitoneal injection of 0.8% pentobarbital sodium (80 $mg.kg^{-1}$). Mid-sagittal images of all caudal intervertebral discs were qualitatively analyzed using MRI to document the structural changes reflected by water molecules. A 7.0 T micro-MRI machine (BioSpec 70/20 USR, Bruker, Germany) was employed to acquire T2-weighted mid-sagittal images and qualitatively analyze T2 mapping of the discs, using a TurboRARE T2-weighted sequence (repetition time = 4000 ms; echo time = 30 ms; field of view =25×25 mm^2; slice thickness = 0.4 mm) and T2 mapping sequence (repetition time = 3000 ms; echo times = 9, 18, 27, 36, 45, 54, 63, 72, 81, 90, 99, 108 ms; field of view = 25×25 mm^2; slice thickness = 0.4 mm). FIJI distribution ImageJ software (v1.54d, National Institutes of Health, USA) was used for manual selection of the region of interest (ROI) for each disc and quantitative analysis of the sagittal T2 image slices. T2 relaxation times were calculated using Image Display and ParaVision (v6.0.1, Bruker, Germany). The MRI index (the average signal intensity) was modified from a previous study to quantify the hydration of the observed disc, with normalization performed against the signal intensity of the upper vertebral bone. The MRI index is defined as:

$$MRI\ index = \frac{Disc\ intensity_n}{Vertebrae\ intensity_{n-1}}$$

where *n* is the level of the disc. The average signal intensity of the disc or vertebrae was quantified using ImageJ.

Micro-CT scanning

The specimen of the spine from L1 to the tail end were harvested from one-month-old mice. After removing the skin and soft tissues, we fixed the specimen in 4% PFA. Subsequently, we scanned it using a micro-CT system (Skyscan 1272, Bruker, Germany) with a resolution of 5 μm, 1300 ms exposure time, 65 kV source voltage, and 153 μA source current along with a 0.25 mm aluminum filter. A total of 385 scanning layers were obtained with a 360-degree rotation and 3D

386 reconstructions were generated by the 3-matic Medical software (v17.0, Materialise, Belgium). The
387 width and height for each vertebra were measured along the mid-sagittal plane, and the volume was
388 calculated using the integral algorithm in HyperMesh software (Release 2022, Altair, USA). These
389 scanning layers were then used to establish a finite element model for simulating the motion of the
390 mouse tail. The relative disc height index and disc convexity index were calculated according to a
391 previous study(59). To quantitatively evaluate the disc height, 10 specimens of coccygeal vertebrae
392 from Co2 to Co8 were harvested from one-month-old mice. To maintain the original morphology
393 of the disc, the fixed samples were scanned using a high-resolution micro-CT system (Skyscan 1276,
394 Bruker, Germany) with a pixel size of 10 μm, 1,014 ms exposure time, 50 kV source voltage, and
395 200 μA source current along with a 0.25 mm aluminum filter. Measurements of volume and
396 moments were performed using CTan software (v1.20). The relative disc height (DH) for each disc
397 was calculated along the mid-sagittal plane according to a previous study(60).

398 $$DH = \frac{Area \times 2}{Width_{upper} + Width_{lower}}$$

399 Where the *area* was calculated between the cephalic and endplates and the *width* included the upper
400 and lower edges of disc. Measurements were repeated at least three times to obtain an average for
401 each disc.
402

403 **Histological analysis**

404 A total of 106 mouse spines were collected for histological profiling purposes. Specifically, 10
405 spines at postnatal day 0 (P0), 12 spines at P3, 16 spines at P7, 13 spines at P14, 29 spines at one
406 month (1M), 14 spines at 3M, and 12 spines at 12M were taken. The mice in each group were
407 obtained from at least three littermates. The spines were cut off at the sacral region, and the levels
408 of the coccygeal disc were determined based on the last sacral vertebra. The surrounding connective
409 tissues, including tendon, muscle, and fascia, were carefully removed to obtain the discs and
410 vertebrae. After that, the specimens from Co2-8 were dissected, fixed in 4% paraformaldehyde for
411 48 hours, then decalcified in EDTA decalcifying solution (R1171, Solarbio) for 20 days before being
412 embedded in paraffin. In the case of disc specimens, tissues were sectioned to the sagittal plane at a
413 thickness of 3 μm in a serial manner, and the gross area of the NP was continuously measured under
414 a microscope. The largest section, or the middle one of the largest sections, was selected for staining

415 analysis and subsequent quantitative assessments. In the case of whole spine specimens, tissues
416 were straightened before fixation to ensure that the middle sagittal views of all discs were aligned
417 at the same focal plane. The sections were stained using hematoxylin and eosin (E607318, Sangon,
418 China), Picro-Sirius Red (G1472, Solarbio, China) for visualization of collagen content or Safranin-
419 O/ Fast Green (G1371, Solarbio, China) for histological assessment. The stained images of the discs
420 were examined under a microscopy system (CX43, Olympus, Japan) and analyzed using FCSnap
421 (V1.1.21486, Olympus, Japan). For the spine from Co2 to Co8, the staining pictures were captured
422 by the VS200 system (Olympus, Japan) and analyzed using OlyVIA software (V3.4.1, Olympus,
423 Japan). The qualification of collagen composition was determined according to a previous study(61).
424 The thickness of fibers in a Picro-Sirius Red staining picture was determined by the value of green,
425 yellow, or red pixels for each point, with green representing thin fibers, yellow representing
426 intermediate fibers, and red representing thick fibers. The region of interest (ROI) was manually
427 selected to distinguish between the NP and AF compartment using ImageJ. To perform Safranin-
428 O/Fast Green staining, the paraffin sections were rehydrated, and then stained with hematoxylin,
429 fast green, and safranin for 5 min successively. Finally, the slides were dehydrated and sealed.
430 To evaluate morphological changes in coccygeal discs, mid-sagittal sections were scored using two
431 histological reference system. The changes in three components including NP, AF, and EP were
432 determined according to the detailed guidelines by four blinded observers(20, 62). The histological
433 scores for each disc were accumulated from all indicators and averaged by the observers.
434 Additionally, a modified Thompson grading system was applied for evaluating the gross
435 morphological changes in NP and AF(21, 63, 64). Discs were graded into five categories by four
436 blinded observers and the final Thompson grades for each disc were determined by the most voted
437 values. In order to reduce observer variation, intra-observer and inter-observer agreement values
438 were calculated using Fleiss' Kappa in R function *kappam.fleiss*. Measurements with $\kappa > 0.6$ were
439 considered to have substantial agreement and valid for statistical analysis.
440
441 **Immunofluorescence staining**
442 For immunostaining, deparaffinized sections were initially treated with Endogenous Peroxidase
443 Blocking Buffer (P0100A, Beyotime, China) for 8 minutes, followed by pepsin retrieval (ZLI9013,
444 ZSGB-BIO, China) for 15 minutes and permeabilization with 1% Triton X-100 (Solarbio, T8200,

445 China) for 15 minutes. Subsequently, the sections were blocked with 5% bovine serum albumin
446 (Sigma, B2064, USA) for 30 minutes. Mouse disc specimens were sectioned at a thickness of 3 μm
447 for immunostaining of Aggrecan (1:100, 13880-1-AP, Proteintech, China), TRPV4 (1:100, PA5-
448 41066, Invitrogen, USA), and PIEZO1 (1:100, 15939-1-AP, ThermoFisher, USA). It is important to
449 note that specimen immunostaining of Brachyury/T (1:50, ab209665, Abcam, UK), EPCR (1:100,
450 ab300523, Abcam, UK), and Col II (1:50, ab185430, Abcam, UK) were embedded in OCT (4583,
451 Sakura) and cryosectioned at a thickness of 10 μm using the Cryostar NX50 (Thermo Scientific,
452 USA). The primary antibody was directly incubated with frozen sections for 6 hours at 4℃ for
453 immunofluorescence staining. Finally, an antifade mounting medium with DAPI solution (Beyotime,
454 P0131, China) was used to visualize the cell nucleus. The immunostaining images were captured
455 using the microscopy system (CX43, Olympus, Japan) and the confocal microscopy system
456 (LSM900, ZEISS, Germany), and analyzed with Zen software (v2.3, ZEISS, Germany) and ImageJ
457 software.
458
459 **Immunohistochemistry staining**
460 Mouse disc specimens were immunostained with primary antibodies against IL-1β (1:200, NOVUS,
461 nb600-633, USA) and MMP3 (1:100, A22328, Abclonal, China). The sections underwent antigen
462 retrieval in a sodium citrate solution (65°C for 150 minutes), followed by blocking with an
463 Endogenous Peroxidase Blocking Buffer for 8 min and incubation in a 5% BSA mixture with 0.3%
464 Triton X-100 for 30 minutes. Subsequently, the sections were exposed to the primary antibodies
465 overnight at 4°C, processed using a polymer HRP detection system (PV9001, GB-BIO, China), and
466 visualized with a DAB peroxidase substrate kit (ZLI-9017, ZSGB-BIO, China). After staining with
467 hematoxylin for nuclear visualization, the sections were mounted with neutral gum. ImageJ software
468 was used to quantify the density of the positive signal.
469
470 **Bulk RNA sequencing**
471 *RNA isolation and sequencing*
472 Coccygeal discs from twenty-five one-month-old mice were classified into type A and type C
473 through micro-MRI before dissection. The surrounding ligaments and muscle of the vertebral
474 column were removed to expose the discs. Coccygeal disc tissues (Co2/3 - Co7/8) were collected

and placed in separate RNA-free tubes on ice (n = 4 - 6 discs for each library) with RNA later reagent (Invitrogen, AM7021, USA). The total RNA for each library was extracted using the MGIEasy RNA toolkit (v3.0, BGI, China). Quality control and abundance for each sample were evaluated using an Agilent 2100 (USA). Equivalent RNA was reversed to cDNA by RT-PCR and then subjected to amplification. The final adapter-ligated cDNA fragments were sequenced on the MGISEQ-2000 platform in a PE150 manner (BGI, China). Reads were aligned to the mouse reference genome (GRCm38) using STAR software (v2.7.1), resulting in a gene-count matrix. Gene expression was quantified as transcripts per million reads (TPM).

RNA-seq data analysis

DESeq2 (v1.34.0) package was employed to analyze RNA-seq data. The data dispersion was estimated using the variance stabilizing transformation (VST) function, and hierarchical clustering was conducted based on the Euclidean distance between samples. Principal Component Analysis (PCA) was used for reduced-dimensional visualization. The differentially expressed genes (DEGs) between the two groups were identified using Wald significance tests with the fitting type set as "mean". Significant DEGs were filtered based on the criterion of log2Foldchange greater than 1 and an adjusted *P* value less than 0.01. In total, 255 upregulated DEGs and 424 downregulated DEGs in type C discs were retained (table S1).

Gene ontology enrichment was performed on DEGs using enrichGO function in clusterProfiler package (v4.2.2). The enriched terms were clustered and visualized using treeplot function in enrichplot package (v1.18.3). GSVA package (v1.42.0) was used to evaluate the scores of gene sets selected from the Molecular Signature Database (MsigDB v2023.1, https://www.gsea-msigdb.org/gsea/msigdb/). Matrisome characteristics were evaluated based on a previous study(65), and the mean scores for each gene set were visualized using the ggradar package (v0.2).

WGCNA analysis

The log2-transformed TPM matrix was utilized for WGCNA analysis (v1.72.1). Genes expressed in at least half of the samples were retained for the automatic network construction and module detection using *blockwiseModules* function, with the power parameter set to 9. The topological overlapped values were calculated for the hierarchical clustering of modules with *minModulesize*

set to 50. Modules with dendrogram heights below 0.4 were merged, and correlations of eigengenes for each module were calculated. The memberships of module eigengenes with respect to groups were quantified, and the significance of modules was determined by calculating the *P* values of the memberships.

Correlation analysis

The RNA-seq expression matrices (GSE100934, GSE128402 and GSE145649) and microarray matrices (GSE134955) were utilized to compare similarities with RNA-seq data from two types of discs. Prior to the comparison, the datasets were first normalized by transforming the count matrices into TPM matrices based on the gene length. Then, Pearson correlation analysis was performed between samples, and the correlation coefficients were visualized using the pheatmap package (v1.0.12).

Single cell RNA sequencing

Single-cell suspension preparation

Twenty one-month-old mice were first examined under MRI scanning to determine the type of disc in the coccygeal spine ranging from Co2/3 to Co7/8. Then, NP and AF tissues from 30 type A and 30 type C discs were harvested and cut into 1 mm^3 pieces in DMEM medium with 10% fetal bovine serum (FBS, Gibco) and 1% Penicillin-Streptomycin solution (P/S, SV30010, Hyclone) for preparation of single cell suspension respectively. Briefly, the ground disc tissues were digested in DMEM supplemented with an enzyme mixture including 0.2% (w/v) pronase (P0652, Sigma-Aldrich), 0.2% (w/v) collagenase P (11213865001, Sigma-Aldrich) and 100 U/ml hyaluronidase (H8030, Solarbio). The digestion was incubated at 37℃ for 40 minutes until the tissues were completely dispersed. The digestion was incubated at 37℃ for 2 hours until the tissues were completely dispersed. PBS with 2% FBS was used to terminate the digestion and filtered through 40 μm filters with a volume ratio of 1:1. Subsequently, the cell suspension was treated with 1× Red Blood Cell Lysis Solution (130-094-183, Miltenyi). Cell viability was tested by AO/PI staining using the Rigel S2 Cell Counter (Countstar, China).

Library construction, sequencing and preprocessing

535 scRNA-seq libraries for mouse discs were constructed using a DNBelab C Series Single-Cell
536 Library Prep Set (940-001924-00, MGI, China). The process includes single cell encapsulation,
537 mRNA capture, reverse transcription, and cDNA amplification in droplet emulsion. Libraries for
538 each sample were indexed and sequenced using a MGISEQ-2000 sequencer (MGI, China). Raw
539 reads embedded in fastq files were preprocessed using the pipeline of DNBelab C Series HT single
540 cell analysis software (https://github.com/MGI-tech-
541 bioinformatics/DNBelab_C_Series_HT_scRNA-analysis-software, V1.2). The mouse reference
542 genome GRCm38 and gene annotation (Release M23) downloaded from GENCODE database were
543 used to align the reads and quantify gene expression. Count matrices were generated after filtering
544 out low-quality reads with default parameters. For quality control, we applied scDblFinder (v1.8.0)
545 to filter out putative doublets for each data set, and cells with more than 1,000 expressed genes and
546 mitochondrial gene counts less than 10% of all counts were retained for downstream analysis.
547
548 *Integration, dimensionality reduction, and clustering*
549 The Seurat (v4.3.0) workflow was used for integrating data set, performing dimensionality reduction,
550 and clustering. Data normalization was performed using the *NormalizeData* function with a
551 *scale.factor* of 10,000. Highly variable genes of the merged data set were calculated using the *vst*
552 method and used to obtain the top 50 principal components (PCs). The *bbknn* function implemented
553 in the bbknnR package (v1.0.2) was used to align batches by using the merged nearest neighbours
554 for cells in each batch, with the *neighbors_within_batch* set to 3. The corrected neighbourhood
555 graph of bbknn was then used to perform uniform manifold approximation and projection (UMAP)
556 for dimension reduction. For unsupervised clustering, the "bbknn" graph was used and the
557 *Findcluster* function was performed using the Louvain algorithm with a resolution of 0.3, resulting
558 in seven major clusters. Clusters with obvious heterogeneity were then subclustered, leading to a
559 final of nine cell clusters. The published scRNA-seq data from murine lumbar spine cells traced
560 using Shh-Cre;tdTomato strategy were analyzed. To isolate the cells labeled by the Shh expression,
561 we reconstructed the gene expression matrix by aligning reads to a customized reference genome
562 containing the *tdTomato* gene sequence. The *tdTomato* expression for each cell were binarized using
563 QUBIC2 algorithm(66), resulting in the *in silico* percentages of tdTomato^{+} cells in each cell clusters.
564 The *FindAllMarkers* function implemented in Seurat was used to calculate DEGs among different

clusters. The Wilcoxon test was performed on each gene, and the adjusted P-value for statistical significance was computed. Genes that met the following criteria were considered signature genes: 1) expressed in a minimum of 20% of either of the two tested populations; 2) at least a 0.25-fold difference (log-scale) between the two tested populations; and 3) an adjusted *P* values less than 0.01. The identity for each cell cluster was manually annotated based on the differentially expressed signature genes (table S2), which were canonical for specific cell types or reported in previous studies(14, 15, 31).

Gene ontology and pathway enrichment

Gene ontology terms enriched in NCs and progenitor cells in type C discs were calculated using the clusterProfiler package embedded in the *RunEnrichment* function in the SCP package (v0.5.4, https://github.com/zhanghao-njmu/SCP). DEGs between cell clusters in type A and type C discs were first calculated and filtered with adjusted *P* values less than 0.01. Then, enrichment analysis was performed using the "GO_BP" database. The clusters of genes and top enriched terms were visualized using the *EnrichmentPlot* function in the SCP package. To compare the signatures in cell clusters between the two types of discs, genes related to the inflammatory response (WP222, WikPathways), elastic fibre (R-MMU-1566948, Reactome) and collagen formation (R-MMU-1474290, Reactome) were extracted for evaluation of scores of gene sets using the GSVA package.

Deconvolution analysis

The Scissor package was used to validate the dominating cell clusters in type A and type C discs, as described above. Cell proportion reconstruction for each bulk RNA-seq sample was inferred using the BayesPrism package (v2.1.2)(67). The scRNA-seq dataset was set as the reference, and genes encoding ribosome, hemoglobin, actin, mitochondrial genes, and genes on chromosome X and Y were excluded from the deconvolution process. The *outlier.cut* threshold was set to 0.01 and the *outlier.fraction* threshold was set to 0.1, resulting in a cell cluster proportion table for each bulk RNA-seq sample.

Finite element model

FE model of a mouse spine from L1 to the tail end was constructed. Initially, the mouse tail was

scanned using a micro-CT system as described above. The image files in DICOM format were converted into 3D model construction using the image processing software Mimics. The properties of tissues within the tail, such as muscle and tendon, were identified according to H&E staining and previous descriptions(68), and then used to generate 3D surface models of each tissue type. These 3D surface models were imported into HyperMesh. A tetrahedral mesh was generated for each tissue type, with element size optimized to ensure model accuracy while minimizing computational cost. The mesh was checked for quality using built-in metrics and any problematic areas were manually refined. Material properties were then assigned to each tissue type based on values reported in the literature (Supplementary Table 3). Finally, to simulate the flexions using an implicit method, the lumbar spine was fully constrained to prevent rigid body motion. A pre-loading equivalent to 20% of the maximum force during flexion to the musculature in the mouse FEM. A load was applied as a displacement boundary condition, forcing a 2 mm displacement of the tendon at the base of tail. Three actions including lateroflexion, dorsiflexion and plantarflexion were simulated. The forces and moments for each disc and the von Mises stress on the disc components during the flexion were recorded. PCA was performed on the stress values of NP, AF and EP for each disc along the lateroflexion.

Atomic force microscopy

Freshly isolated disc specimens were embedded in OCT and longitudinally cryosectioned at a thickness of 100 μm. Sections were fixed on the slide using waterproof glue (Pattex) and kept at 4°C to avoid dehydration. AFM measurements were performed on a Dimension Icon Scanasyst with a Nanoscanpe 6 controller (Bruker, Germany). For the indentation test, cantilevers coated with reflective gold (k nom = 1 Nm^{-1}) with a symmetric tip (radius = 20 nm, height = 8 μm) were used (Ready, China). Before scanning, the cantilevers were calibrated utilizing the thermal tune method with a range set at 1-100 KHz and a spring constant set at 1.115 Nm^{-1}. The operation was performed using Nanoscope software (v9.70). The Lorentzian (Air) model was chosen to fit the data. For each disc sample, at least three ROIs were selected for the NP and AF regions under an optical microscope. Each ROI included 25 detection points with a 45-nm spacing. A total of six samples including three type A and three type C discs were measured. Data analysis was performed using the Hertzian model in Nanoscope Analysis software (v3.00). Baseline correction was executed on the extend and retract

curves separately. To obtain the force-distance curves and Young's modulus, indentation analysis was performed with the contact point algorithm set as "Best Estimate" and the Max and Min force fit boundary set at 90% and 30%, respectively. Measurement results with an R value of more than 0.75 were considered valid and retained for subsequent comparative analysis.

Imaging Fourier transform infrared (FTIR) spectrometry analysis

Disc specimens were longitudinally cryosectioned at a thickness of 10 μm and used to perform FTIR imaging analysis on a Nicolet iN10 Infrared Microscope (Thermo Scientific, USA). Briefly, the specimens were placed onto infrared transparent BaF_2 windows. The transmission collection mode was applied using a "Cooled" detector, with a wavenumber range of detection set between 4,000 cm^{-1} and 400 cm^{-1}. A 100 μm length was used to scan the section, and spectral data were collected for four samples from each group using OMNIC Picta software (Thermo Scientific, USA). For each sample, data from at least three detection points in the NP, AF and EP were collected for subsequent analysis using OMNIC software (v9.2.86). Specifically, the transmission rate curves were transformed into absorbance curves for baseline correction and smoothing to remove the noisy peaks. Then, the absorbance data were processed using the prospectr R package (v0.2.6), in which Savitzky-Golay smoothing and second derivative for the absorbance values were calculated using the *savitzkyGolay* function ($m = 2$, $p = 3$, $w = 11$ and *delta.wave* = 2). The resulting derivatives from detection points in one sample were averaged to minimize technical errors, and multiplied by a factor of negative one for positive visualization. The absolute absorbance values for proteoglycan (wavelength = 1,156 cm^{-1}), collagen (wavelength = 1,338 cm^{-1}) and total protein (wavelength = 1,660 cm^{-1}) were extracted for comparative analysis according to previous studies(29, 64).

Mechanical property measurement

Mechanical property measurements were conducted using a Universal Testing Machine (AI-7000-SU1, GOTECH, China) equipped with a load cell of 500 N mechanical capacity at room temperature. In compression testing, functional spine units (FSUs) comprising disc and adjacent vertebrae were freshly isolated with soft tissues removed. The descending speed rate for displacement was set as 0.1 mm/minute, and testing ceased when real-time force dropped to 30% of the maximum force. Force-Displacement curves were generated and used to derive Stress-Strain curves based on the disc

area and height. Lowess Smoothing was applied to reduce the noise in each curve. Mechanical properties such as maximum stress, toe and linear region modulus, transition and maximum strains were calculated. Briefly, for each curve, the transition point distinguishing the toe region and linear region was identified using the segmented R package (v2.0.2). The modulus for these regions indicated by their slopes, were calculated using the *coef* function from fitted linear models of strain and stress. The maximum strain was determined by the peak stress. The disc type was determined according to the histological staining of the test samples. A minimum of 10 samples were tested for each disc type.

In 3-point bending test, double function spine units (dFSU) comprising vertebrae and bilateral discs were segmented, and categorized into dFSU with two type A discs (AA), dFSU with two type C discs (CC) and dFSU with one type A and one type C disc (AC). The spine specimens were placed horizontally on two supports with a rounded surface (R2 = 2 mm), ensuring suspension of the FSUs, with a span distance of 8.0 mm between the lower supports. A metal indenter with a rounded surface (R1 = 2 mm) was centrally positioned between the supports and connected to the load cell. It descended at a rate of 0.1 mm/minute to apply load to the center of the vertebral body. The test concluded when the force in real-time dropped to 30% of the maximum force. Force-Displacement curves were generated, and the bending strength (σ_b) for each test was calculated using the following formula:

$$\sigma_b = \frac{8F_{max} \times l}{\pi \times D^3}$$

Where the F_{max} was the maximum force during testing, l was the span distance, and D was the average transverse diameter of the dFSU. The modulus (E_b) for the 3-point bending test were calculated using the following formula:

$$E_b = \frac{4l^3}{3\pi \times D^4} \times k$$

Where the k was the slope calculated from the fitted linear models on displacement and force. The toe region and linear region in the curves were determined as described above. At least 5 samples were tested for each category of dFSU.

Cyclic compression and tension tests were carried out on locomotion segments (functional spinal units, FSU) using an Instron 5969 machine with a 100 N load cell capacity at room temperature(69). FSUs were bonded using polymethylmethacrylate-coated fixtures and Loctite 401 adhesive with

Loctite SF 770 accelerant, then immersed in physiological saline. Test parameters were set and adjusted based on a previous mouse study(22), with compressive and tensile thresholds at -1 N and 1 N, respectively, a speed of 0.1 mm/s, and an axial pre-load of 0.15 N applied for 1 minute before testing. A total of 10 cycles were performed and the force-displacement curve from the final cycle was fitted using a double sigmoid function, with the 2nd derivative indicating the neutral zone boundaries. The length of the neutral zone, compressive and tensile range of motion, as well as the area of the top and bottom surfaces and height of the FSU, were calculated for statistical analysis. Ten FSUs, including type A or type C discs from 1-month-old mice, were isolated, tested, and stained for disc type identification post-experiment.

Tendon detachment

The impact of mechanical unloading on the mouse tail disc was assessed through tendon detachment. Briefly, neonatal mouse pups were cryo-anesthetized on a paper-lined ice pack for 5 minutes to induce unconsciousness before the surgical procedure(70). Subsequently, two 5 mm incisions were made in the skin of the tail base along the sagittal direction in both ventral and dorsal aspects to avoid damaging blood vessels. The surrounding tendons were delicately separated and excised using razor blades. It is important to note that the skin was sterilized and did not require suturing due to rapid healing observed the following day. Mice in the sham-operated control group had their tendons left intact. All procedures were conducted under microscopic guidance. The pups were then allowed to recover on an incubator with an infrared heater before being returned to their mother's cage. To confirm the efficacy of tendon detachment in preventing tail wagging, mice underwent a treadmill test one-month post-surgery (movie S4). Mice that exhibited no tail movement, even when subjected to electrical stimulation, were retained for histological evaluation. Histological scoring was performed on each disc to characterize its type.

Drug administration

The injection was administered with a 33-gauge needle attached to a Hamilton microsyringe. It was inserted into the skin around the Co6 vertebra and advanced towards the tail base along the sagittal plane. Drugs were manually administered while retracting the needle along the tail axis at a consistent speed. The Trpv4-specific agonist GSK1016790A (HY-19608, MedChemExpress, USA)

714 at a concentration of 10 μM and the Piezo1-specific agonist Yoda1 (HY-18723, MedChemExpress,
715 USA) at a concentration of 500 μM were diluted in 20% SBE-β-CD (HY-17031, MedChemExpress,
716 USA) and 2% DMSO for injection. The dosage of GSK1016790A and Yoda1 for mice of different
717 ages was standardized at 0.1 mg/kg and 1 mg/kg, respectively, according to the recommendations
718 in the instructions. Injections were administered weekly, with a total of four injections performed
719 before harvesting, and subsequent histological staining of the discs ranging from Co2 to Co8.
720
721 **Statistical analysis**
722 All statistical analyses were conducted using R (v4.1.3) and software packages compiled in R
723 language. The significance of DEGs in RNA-seq data was assessed using the *result* function in the
724 DESeq2 package with the "Wald" test parameter. Significance was determined using Student's t-
725 test for the data with homogeneity of variance and normal distribution, and Wilcox-test for the other
726 data. Data points are shown in the barplots and boxplots if the number of replicates is less than 10.
727 Additional statistical analyses are detailed in the corresponding sections of the manuscript.
728 C57BL/6J mice sourced from a minimum of three commercial laboratories were utilized to mitigate
729 the effect of housing environment. Sample sizes were determined to ensure adequate standard
730 deviations of the mean and biologically meaningful differences between experimental groups.
731
732 **Data and materials availability:**
733 The sequencing data including bulk RNA-seq and scRNA-seq supporting the findings of this study
734 were deposited in the National Omics Data Encyclopedia (https://www.biosino.org/node/index)
735 under the accession number OEP004269 and OEP005392. Mouse sequencing data from published
736 references are available at the GEO with the accession code mentioned in the main text. An interface
737 for scRNA-seq data browsing based on ShinyCell is available online (www.ivdatlas.cn:3838/mIVD)
738 (71). There are no restrictions on data availability. All software and packages including the version
739 are provided in the Method. Custom codes used in the data analysis are available on GitHub
740 (https://github.com/hejian41/mouse_IVD).
741
742 **Authors contributions**
743 PLiu, YG, BL and JH conceived and designed the study. YL, LC, and YX provided research

consultation. SH, JH, YG, PY, YLi, OH, and P. Lin prepared the animal specimens. YLi. and QQ performed animal breeding. SH, PY, and YW performed immunohistochemistry and immunofluorescence staining. JH and SH conducted the AFM, FTIR, and FSU testing analysis. YG and JH conducted the FEM analysis. YG, SH, and YG performed radiological experiments. JZ, LZ, HJ, YLiu and XZ provided the clinic specimens. JH analyzed and interpreted the sequencing data. JH, YG, and PLiu designed the figures. YG, JH, BL, and PLiu wrote the manuscript. All authors have read and approved the final manuscript.

Acknowledgments

We thank J. Liu from Jiejun Technique Corporation for his contribution to the FEM construction, W. Ji from Bioengineering College of Chongqing University for assistance during FTIR experiments, and W. Zheng from Olympus Corporation for the help with section staining and imaging. This study was supported by grants from the National Key Research and Development Program of China (2022YFA1103202), the National Natural Science Foundation of China (32270887, 82272507, and 32200654), the Natural Science Foundation of Chongqing (CSTB2023NSCQ-ZDJO008), Postdoctoral Innovative Talent Support Program (BX20220397), the Open Project of State Key Laboratory of Trauma, Burns and Combined Injury (SFLKF202201), Project for Enhancing Innovation of Army Medical University (2023XJS39), and Talent Innovation Training Program at the Army Medical Center (ZXZYTSYS09).

References

1. Sparrey CJ, et al. Etiology of lumbar lordosis and its pathophysiology: a review of the evolution of lumbar lordosis, and the mechanics and biology of lumbar degeneration. *FOC*. 2014;36(5):E1.

2. Plomp KA, Dobney K, Collard M. Spondylolysis and spinal adaptations for bipedalism. *Evolution, Medicine, and Public Health*. 2020;2020(1):35–44.

3. Calvo-Muñoz I, Gómez-Conesa A, Sánchez-Meca J. Prevalence of low back pain in children and adolescents: a meta-analysis. *BMC Pediatr*. 2013;13:14.

4. Cheung KMC, et al. Prevalence and pattern of lumbar magnetic resonance imaging changes in a population study of one thousand forty-three individuals. *Spine (Phila Pa 1976)*. 2009;34(9):934–940.

5. Kalichman L, et al. Computed tomography-evaluated features of spinal degeneration: prevalence,

intercorrelation, and association with self-reported low back pain. *Spine J*. 2010;10(3):200–208.

6. Teraguchi M, et al. Prevalence and distribution of intervertebral disc degeneration over the entire spine in a population-based cohort: the Wakayama Spine Study. *Osteoarthritis Cartilage*. 2014;22(1):104–110.

7. GBD 2021 Low Back Pain Collaborators. Global, regional, and national burden of low back pain, 1990-2020, its attributable risk factors, and projections to 2050: a systematic analysis of the Global Burden of Disease Study 2021. *Lancet Rheumatol*. 2023;5(6):e316–e329.

8. Ravindra VM, et al. Degenerative Lumbar Spine Disease: Estimating Global Incidence and Worldwide Volume. *Global Spine Journal*. 2018;8(8):784–794.

9. O'Connell GD, Vresilovic EJ, Elliott DM. Comparison of Animals Used in Disc Research to Human Lumbar Disc Geometry: *Spine*. 2007;32(3):328–333.

10. Showalter BL, et al. Comparison of Animal Discs Used in Disc Research to Human Lumbar Disc: Torsion Mechanics and Collagen Content. *Spine*. 2012;37(15):E900–E907.

11. Lacava SA, Isilak N, Uusisaari MY. Mice tails function in response to external and self-generated balance perturbation on the roll plane.

12. Hunter CJ, Matyas JR, Duncan NA. Cytomorphology of notochordal and chondrocytic cells from the nucleus pulposus: a species comparison. *Journal of Anatomy*. 2004;205(5):357–362.

13. Ohnishi T, et al. Age-related spontaneous lumbar intervertebral disc degeneration in a mouse model: SPONTANEOUS MOUSE IVD DEGENERATION. *J Orthop Res*. [published online ahead of print: July 9, 2017]. https://doi.org/10.1002/jor.23634.

14. Gan Y, et al. Spatially defined single-cell transcriptional profiling characterizes diverse chondrocyte subtypes and nucleus pulposus progenitors in human intervertebral discs. *Bone Res*. 2021;9(1):37.

15. Lin P, et al. Spatially multicellular variability of intervertebral disc degeneration by comparative single-cell analysis. *Cell Prolif*. 2023;e13464.

16. Bagi CM, et al. The use of micro-CT to evaluate cortical bone geometry and strength in nude rats: correlation with mechanical testing, pQCT and DXA. *Bone*. 2006;38(1):136–144.

17. Janz KF, et al. Objectively measured physical activity trajectories predict adolescent bone strength: Iowa Bone Development Study. *Br J Sports Med*. 2014;48(13):1032–1036.

18. Sarver JJ, Elliott DM. Mechanical differences between lumbar and tail discs in the mouse. *J Orthop Res*. 2005;23(1):150–155.

19. Lambers FM, et al. Mouse tail vertebrae adapt to cyclic mechanical loading by increasing bone formation rate and decreasing bone resorption rate as shown by time-lapsed in vivo imaging of dynamic bone morphometry. *Bone*. 2011;49(6):1340–1350.

20. Melgoza IP, et al. Development of a standardized histopathology scoring system using machine learning algorithms for intervertebral disc degeneration in the mouse model—An ORS spine section initiative. *JOR Spine*. 2021;4(2):e1164.

21. Thompson JP, et al. Preliminary Evaluation of a Scheme for Grading the Gross Morphology of the Human Intervertebral Disc: *Spine*. 1990;15(5):411–415.

22. Choi H, et al. A novel mouse model of intervertebral disc degeneration shows altered cell fate and matrix homeostasis. *Matrix Biology*. 2018;70:102–122.

23. Shapiro IM, Risbud MV. Transcriptional profiling of the nucleus pulposus: say yes to notochord. *Arthritis Res Ther*. 2010;12(3):117.

24. Rodrigues-Pinto R, et al. Spatiotemporal analysis of putative notochordal cell markers reveals CD24 and keratins 8, 18, and 19 as notochord-specific markers during early human intervertebral disc development. *J Orthop Res*. 2016;34(8):1327–1340.

25. Fine N, et al. Intervertebral disc degeneration and osteoarthritis: a common molecular disease spectrum. *Nat Rev Rheumatol*. 2023;19(3):136–152.

26. Peck SH, et al. Whole Transcriptome Analysis of Notochord-Derived Cells during Embryonic Formation of the Nucleus Pulposus. *Sci Rep*. 2017;7(1):10504.

27. Liu Z, et al. Dysregulation of STAT3 signaling is associated with endplate-oriented herniations of the intervertebral disc in Adgrg6 mutant mice. *Plos Genet*. 2019;15(10):e1008096.

28. Wei L, et al. Chondroitin synthase-3 regulates nucleus pulposus degeneration through actin-induced YAP signaling. *Faseb J*. 2020;34(12):16581–16600.

29. Novais EJ, et al. Long-term treatment with senolytic drugs Dasatinib and Quercetin ameliorates age-dependent intervertebral disc degeneration in mice. *Nat Commun*. 2021;12(1):5213.

30. Ou X, O'Leary HA, Broxmeyer HE. Implications of DPP4 modification of proteins that regulate stem/progenitor and more mature cell types. 2013;122(2).

31. Tu J, et al. Single-Cell Transcriptome Profiling Reveals Multicellular Ecosystem of Nucleus Pulposus during Degeneration Progression. *Adv Sci*. 2021;22.

32. Wang H, et al. Decoding the annulus fibrosus cell atlas by scRNA-seq to develop an inducible composite hydrogel: A novel strategy for disc reconstruction. *Bioact Mater*. 2022;14:350–363.

33. Zhang C, et al. Single cell RNA sequencing reveals emergent notochord-derived cell subpopulations in the postnatal nucleus pulposus. *FASEB J*. 2024;38(1):e23363.

34. Bishop PJ, et al. Predictive simulations of running gait reveal a critical dynamic role for the tail in bipedal dinosaur locomotion. *Sci Adv*. 2021;7(39):eabi7348.

35. Wang L, et al. Innovative design of minimal invasive biodegradable poly(glycerol-dodecanoate)

842 nucleus pulposus scaffold with function regeneration. *Nat Commun*. 2023;14(1):3865.

843 36. Gilchrist CL, et al. TRPV4-mediated calcium signaling in mesenchymal stem cells regulates
844 aligned collagen matrix formation and vinculin tension. *Proc Natl Acad Sci USA*.
845 2019;116(6):1992–1997.

846 37. Syeda R, et al. Chemical activation of the mechanotransduction channel Piezo1. *eLife*.
847 2015;4:e07369.

848 38. Zhang Y, et al. Lufengpithecus inner ear provides evidence of a common locomotor repertoire
849 ancestral to human bipedalism. *The Innovation*. 2024;5(2):100580.

850 39. Pocovi NC, et al. Effectiveness and cost-effectiveness of an individualised, progressive walking
851 and education intervention for the prevention of low back pain recurrence in australia (WalkBack):
852 A randomised controlled trial. *Lancet*. 2024;404(10448):134–144.

853 40. Micheli LJ. Back Pain in Young Athletes: Significant Differences From Adults in Causes and
854 Patterns. *Arch Pediat Adol Med*. 1995;149(1):15.

855 41. Jensen MC, et al. Magnetic Resonance Imaging of the Lumbar Spine in People without Back
856 Pain. *N Engl J Med*. 1994;331(2):69–73.

857 42. Chen C, et al. Autologous fibroblasts induce fibrosis of the nucleus pulposus to maintain the
858 stability of degenerative intervertebral discs. *Bone Res*. 2020;8(1):7.

859 43. Alini M, et al. Are animal models useful for studying human disc disorders/degeneration? *Eur*
860 *Spine J*. 2008;17(1):2–19.

861 44. Xia B, et al. On the genetic basis of tail-loss evolution in humans and apes. *Nature*.
862 2024;626(8001):1042–1048.

863 45. Reilly SM, McElroy EJ, Biknevicius AR. Posture, gait and the ecological relevance of locomotor
864 costs and energy-saving mechanisms in tetrapods. *Zoology (Jena)*. 2007;110(4):271–289.

865 46. Lacava SA, Isilak N, Uusisaari MY. Mice tails function in response to external and self-
866 generated balance perturbation on the roll plane [preprint]. 2024.
867 https://doi.org/10.1101/2024.04.18.589832.

868 47. Stokes IAF, Iatridis JC. Mechanical conditions that accelerate intervertebral disc degeneration:
869 overload versus immobilization. *Spine (Phila Pa 1976)*. 2004;29(23):2724–2732.

870 48. Kim MK, Ramachandran R, Séguin CA. Spatiotemporal and functional characterisation of
871 transient receptor potential vanilloid 4 (TRPV4) in the murine intervertebral disc. *Eur Cell Mater*.
872 2021;41:194–203.

873 49. Walter BA, et al. Reduced tissue osmolarity increases TRPV4 expression and pro-inflammatory
874 cytokines in intervertebral disc cells. *Eur Cell Mater*. 2016;32:123–136.

875 50. Easson GWD, et al. TRPV4 differentially controls inflammatory cytokine networks during static
876 and dynamic compression of the intervertebral disc. *JOR Spine*. 2023;6(4):e1282.

877 51. Mark Kim MK, et al. Transient receptor potential vanilloid 4 regulates extracellular matrix
878 composition and mediates load-induced intervertebral disc degeneration in a mouse model.
879 *Osteoarthritis Cartilage*. 2024;32(7):881–894.

880 52. Cambria E, et al. TRPV4 mediates cell damage induced by hyperphysiological compression and
881 regulates COX2/PGE2 in intervertebral discs. *JOR Spine*. 2021;4(3):e1149.

882 53. Easson GWD, et al. Modulation of TRPV4 protects against degeneration induced by sustained
883 loading and promotes matrix synthesis in the intervertebral disc. *FASEB J*. 2023;37(2):e22714.

884 54. Mark Kim MK, et al. Transient receptor potential vanilloid 4 regulates extracellular matrix
885 composition and mediates load-induced intervertebral disc degeneration in a mouse model.
886 *Osteoarthritis Cartilage*. 2024;32(7):881–894.

887 55. Easson GWD, et al. Modulation of TRPV4 protects against degeneration induced by sustained
888 loading and promotes matrix synthesis in the intervertebral disc. *FASEB J*. 2023;37(2):e22714.

889 56. Suzuki M, et al. Impaired pressure sensation in mice lacking TRPV4. *J Biol Chem*.
890 2003;278(25):22664–22668.

891 57. Krupkova O, Zvick J, Wuertz-Kozak K. The role of transient receptor potential channels in joint
892 diseases. *Eur Cell Mater*. 2017;34:180–201.

893 58. Kim MK, Ramachandran R, Séguin CA. Spatiotemporal and functional characterisation of
894 transient receptor potential vanilloid 4 (TRPV4) in the murine intervertebral disc. *Eur Cell Mater*.
895 2021;41:194–203.

896 59. Kunkel ME, et al. Morphometric analysis of the relationships between intervertebral disc and
897 vertebral body heights: an anatomical and radiographic study of the human thoracic spine:
898 Morphometric analysis of the relationships between intervertebral disc and vertebral body heights.
899 *J Anat*. 2011;219(3):375–387.

900 60. Nishimura K, Mochida J. Percutaneous Reinsertion of the Nucleus Pulposus: An Experimental
901 Study. *Spine*. 1998;23(14):1531–1538.

902 61. Johnston SN, et al. Conditional Deletion of HIF -2α in Mouse Nucleus Pulposus Reduces
903 Fibrosis and Provides Mild and Transient Protection From Age-Dependent Structural Changes in
904 Intervertebral Disc. *J of Bone & Mineral Res*. 2022;37(12):2512–2530.

905 62. Tam V, et al. Histological and reference system for the analysis of mouse intervertebral disc:
906 HISTOLOGICAL GRADING OF MOUSE DISC. *J Orthop Res*. [published online ahead of print:
907 July 18, 2017]. https://doi.org/10.1002/jor.23637.

908 63. Bedore J, et al. Impaired Intervertebral Disc Development and Premature Disc Degeneration in

Mice With Notochord-Specific Deletion of CCN2. *Arthritis Rheum*. 2013;65(10):2634–2644.

64. Tessier S, et al. TonEBP-deficiency accelerates intervertebral disc degeneration underscored by matrix remodeling, cytoskeletal rearrangements, and changes in proinflammatory gene expression. *Matrix Biol*. 2020;87:94–111.

65. Naba A, et al. The extracellular matrix: Tools and insights for the “omics” era. *MATRIX BIOLOGY*. 2016;49:10–24.

66. Xie J, et al. QUBIC2: a novel and robust biclustering algorithm for analyses and interpretation of large-scale RNA-Seq data. *Bioinformatics*. 2020;36(4):1143–1149.

67. Chu T, et al. Cell type and gene expression deconvolution with BayesPrism enables Bayesian integrative analysis across bulk and single-cell RNA sequencing in oncology. *Nat Cancer*. 2022;3(4):505–517.

68. Shinohara H. The Musculature of the Mouse Tail is Characterized by Metameric Arrarmements of Bicipital Muscles. *Okajimas Folia Anatomica Japonica*. 1999;76(4):157–169.

69. Torre OM, et al. Biomechanical test protocols to detect minor injury effects in intervertebral discs. *J Mech Behav Biomed Mater*. 2019;95:13–20.

70. Malek Mohammadi M, Abouissa A, Heineke J. A surgical mouse model of neonatal pressure overload by transverse aortic constriction. *Nat Protoc*. 2021;16(2):775–790.

71. Ouyang JF, et al. ShinyCell: simple and sharable visualization of single-cell gene expression data. *Bioinformatics*. 2021;37(19):3374–3376.

Conflict of interest: Authors declare that they have no competing interests

Figure 1. Histological profiling of mouse coccygeal spine identifies spatiotemporal characteristics of the disc.

(**A**) Schematic illustrating the design of the profiling study. A total of 106 coccygeal spines from neonatal to mid-aged C57BL/6J mice were collected for histological profiling and evaluation using a scoring system. The integration of micro-CT (μCT), magnetic resonance imaging (MRI) and Fourier transform infrared spectrometer (FTIR) facilitates the identification of distinguishing characteristics of two types of discs.

(**B**) Representative sagittal views of safranin O/Fast green (SOFG) staining on coccygeal spine spanning from Co2 (proximal) to Co8 (distal) across various postnatal developmental stages. The samples include P0 (postnatal day 0, N = 10), P3 (N = 12), P7 (N = 16), P14 (N = 13), P28 (N = 29), 3M (3-month-old, N = 14), and 12M (N = 12). Cartilage is depicted in red, while fibers and bones are shown in blue. The longitudinal growth of the spine is accompanied by fibrous and osteogenic deposition in vertebrae and chondrogenic deposition in discs.

(**C**) The heights of discs from Co2/3 to Co7/8 levels were measured at various developmental time points. Data are mean ± S.E.; Right, detailed comparison of disc levels at P28, 3M and 12M. The central line represents the median, boxes indicate 25th–75th interquartile range and whiskers 1.5*interquartile range. *P* values are determined by Kruskal-Wallis test.

(**D**) Histopathological scores of discs from Co2/3 to Co7/8 levels were calculated at various developmental time points. Data are mean±S.E.; Right, detailed comparison of different disc levels at P28, 3M and 12M. *P* values are determined by Kruskal-Wallis test.

(**E**) Grade distributions of nucleus pulposus (NP, top) and annulus fibrosus (AF, bottom) in discs at various developmental time points (left) and anatomic levels (right), using a modified Thompson grading system reliant on the SOFG staining.

(**F**) Representative sagittal views (left) of a 7.0T microMRI image depict a T2-weighted image and relaxation time of the mouse coccygeal spine. Discs from Co2 to Co8 are labeled with gray values and a pseudo-color map indicating the water content in the tissues. MRI index (right) values of mouse coccygeal discs from Co2/3 to Co7/8. *P* value is determined by Kruskal-Wallis test. Segmented line in matching colors denotes discs from the same mouse (N = 47). The dark point represents the means and the line indicates 95% confidence interval.

962

963 **Figure 2. Multilayer-characterization of collagen-abundant disc in mouse tail base.**

964 (**A**) Representative horizontal sections of discs ranging from Co2/3 to Co7/8, in which NP region
965 of Co2/3, Co6/7, and Co7/8 exhibit gelatinous and enriched water content, while those of Co3/4,
966 Co4/5, and Co5/6 exhibit non-gelatinous and decreased water content. Scale bar, 1 mm.

967 (**B**) Representative sagittal section of SOFG and hematoxylin-eosin (H&E) staining showed the
968 distinct morphology of Co7/8 and Co4/5 discs. Dashed lines indicate the boundary between NP and
969 AF. Scale bar, 100 μm.

970 (**C**) Representative picture of Picrosirius Red staining on Co7/8 and Co4/5 discs under bright field
971 (left) and polarized light (right). The collagen fiber thickness is denoted by green (Thin), yellow
972 (Intermediate), and red (Thick).

973 (**D**) Violin plots display the collagenic area proportions identified by Picrosirius Red staining in NP
974 from two group sets of discs (N = 10 for each group set). Co4/5 disc with NP fulfilled with collagen
975 fiber. *P* values of significance are determined by two-tailed Student's t-test. Each point represents
976 the average value from discs in the same group set within individual mice (N = 10).

977 (**E**) Stacked bar charts show the collagen fiber composition in AF of Co7/8 and Co4/5 discs. *P*
978 values of significances between two types of discs are determined by two-tailed Fisher's exact tests.

979 (**F**) Representative FTIR images of Co7/8 and Co4/5 discs. The color gradient indicates the relative
980 absorbance levels of collagen (1338 cm^{-1}).

981 (**G**) Spectrum diagram of average second derivatives of absorbance peak across wavelengths from
982 1,000 cm^{-1} to 1,800 cm^{-1} in the NP region (top) and AF region (bottom) from Co7/8 and Co4/5 discs.
983 Derivatives at 1156 cm^{-1} (proteoglycan), 1338 cm^{-1} (collagen) and 1668 cm^{-1} (total protein) are
984 indicated by dashed lines.

985 (**H**) Violin plots show the derivatives at three wavelengths of NP or AF from two type of discs (N =
986 10 for each group). *P* values of significance are determined by two-tailed Student's t-test. Points
987 represent values at 3 detection points from an individual disc (N = 5).

988 (**I**) Stacked bar charts show the frequency of two types of discs across Co2/3 to Co7/8. The types of
989 discs are identified according to the SOFG staining for each sample, resulting in type A (aggrecan-
990 abundant) and type C (collagen-abundant) discs. The dashed line indicates the average proportion
991 of type C discs in all samples (N = 35).

992 (**J**) Summarized table comparing distinct characteristics in type A and type C discs.

993

994 **Figure 3. Type C disc does not feature the degeneration characteristics.**

995 (**A**) PCA of type A and type C discs (N = 6 for each group). The PC1 (explaining 74% of the variance)
996 and PC2 (explaining 13% of the variance) are set as the axes.

997 (**B**) Heatmap shows the expression (column scaled) of significant DEGs between the two types of
998 discs. DEGs are hierarchically clustered into two branches based on the expression levels.

999 (**C**) GSEA analysis of core matrisome term (Collagens) in upregulated genes of type C discs.
1000 Enriched genes in term are labelled.

1001 (**D**) Expression levels of *Col2a1, Col1a1* and *Acan*. Box indicates 25th, median (middle line), 75th
1002 quartiles, and whiskers indicate 5th and 95th percentiles and single points indicate outliers. *P* values
1003 of significance are determined by the Wilcoxon rank-sum test.

1004 (**E**) Representative immunofluorescent staining of ACAN and COL II in type A and type C discs
1005 (left). Quantification of signaling density in NP region and AF region (right). Scale bar, 100 μm. *P*
1006 values were calculated with two-tailed Student's t-tests.

1007 (**F**) Volcano map shows the log2-transformed foldchanges and negatively log10-transformed
1008 adjusted *P* values for all genes, indicated by the color gradient. Curated significant DEGs are
1009 highlighted.

1010 (**G**) Radar map shows the performance of six gene sets associated with the indicated functions and
1011 metabolic pathways in the two types of discs.

1012 (**H**) Expression levels of inflammatory factor gene *Il1b* and degenerative marker gene *Mmp3*.

1013 (**I**) Representative immunohistology staining of IL-1β and MMP3 in type A and type C discs. Scale
1014 bar, 100 μm. Proteins are brown, and nuclei are blue. *P* values were calculated with Student's t-tests.

1015 (**J**) Expression levels of apoptotic genes *Bcl2* and *Bax*.

1016

1017 **Figure 4. Mechanical properties of type C discs.**

1018 (**A**) Schematic of AFM analysis on the horizontal surface of discs. Two processes including
1019 indentation and retraction are conducted and recorded to generate force-distance curves.

1020 (**B**) Representative force-distance curves were detected in the NP region (left) and AF region (right)
1021 from type A (top) and type C (bottom) discs.

1022 (**C**) The stiffness reflected by Young's modulus was calculated from each test. Data are shown with
1023 mean and 95% confidence interval. Two-tailed Student's t-tests are used to determine the *P* values.
1024 The point represents 25 tests from the individual sample (N = 4).
1025 (**D**) Schematic of mechanical property testing. In compression test, FSU consists of the entire disc
1026 and adjacent vertebrae. The FSU bears the force from the load cell. In 3-point bending test, dFSU
1027 comprises a vertebra sandwiched by two discs. The load cell exerts a force on the middle of the
1028 dFSU. The force and displacement are meticulously recorded during the test.
1029 (**E**) Representative stress-strain curves detected in compression test on type A and type C discs (left).
1030 Quantification of maximum stress in each test (right, N = 10 for each group).
1031 (**F**) Quantification of the toe and linear region modulus (N = 10 for each group).
1032 (**G**) Quantification of transition and maximum strains. Data are shown as means ± S.E. (N = 10 per
1033 group). Significant differences between groups were assessed via two-tailed Student's t-tests.
1034 (**H**) Representative stress-strain curves detected in 3-point bending test on type A and type C discs
1035 (left). Quantification of maximum stress in each test (right, N = 10 for each group).
1036 (**I**) Quantification of the toe and linear region modulus (N = 10 for each group).
1037 (**J**) Quantification of transition and maximum strains. Data are shown as means ± S.E. (N = 10 for
1038 each group). Significant differences between groups were assessed with the Wilcoxon rank-sum test.
1039 (**K**) Representative of last force-displacement curve. Red dots and blue dots indicate compressive
1040 and tensile process respectively. NZ, neutral zone; ROM, range of motion.
1041 (**L**) Quantification of NZ length (normalized to FSU length), axis ROM (normalized to FSU length),
1042 stiffness, and NZ stiffness in compressive and tensile process. Data are shown as means ± S.E. (N
1043 = 10 for each group). Significant differences between groups were assessed with the Wilcoxon rank-
1044 sum test.
1045
1046 **Figure 5. scRNA-seq analysis reveals the cellular alterations and enhanced chondrogenesis in**
1047 **type C discs.**
1048 (**A**) The Uniform Manifold Approximation and Projection (UMAP) plot depicts the cell clusters
1049 identified in two distinct disc types, including Notochord cells (NC), regulatory chondrocytes
1050 (RegC), hypertrophic chondrocytes (HyperC), fibrotic chondrocytes (FibroC), cycling chondrocytes
1051 (CycC), osteoprogenitors (OP), and progenitor cells (PC).

(**B**) Expression of marker genes was used to identify the cell clusters. Color gradient indicates the average gene expression in clusters. Dot size indicates the percentage of gene expression within each cluster.

(**C**) Percentages of each cell cluster in type A and type C discs.

(**D**) Representative immunofluorescent staining of NC marker Brachyury (*T*) and PC marker EPCR (*Procr*) in type A and type C discs (top). Quantification of T^+ cell and $PROCR^+$ cells in NP and AF region (bottom). Scale bar, 100 μm. *P* values were calculated with two-tailed Student's t-tests.

(**E**) Top 10 differentially expressed genes in NCs and PCs between type A and type C discs.

(**F**) Volcano maps of DEGs in chondrocyte clusters between type A and type C discs. Color gradient indicates the P values of each gene. Curated significant DEGs are highlighted.

(**G**) KEGG analysis of upregulated genes in type C chondrocyte clusters. The enriched signaling pathway for each cluster are shown in the dot plot. Color gradient indicates the *P* values of enrichment. Dot size indicates the ratio of enriched genes to all genes in the pathway.

(**H**) UMAP of disc and VB cell clusters by re-analyzing scRNA-seq dataset of mouse lumbar spine.

(**I**) UMAP of tdTomato gene expression in disc and VB cell clusters.

(**J**) The expression of tdTomato gene were binarized using QUBIC2 algorithm. The composition of $tdTomato^+$ and $tdTomato^-$ cells for each cell clusters were calculated.

Figure 6. Mechanical stress is essential for the formation of type C discs.

(**A**) Vertical view of FEM of mouse vertebrae. Colored vertebral bodies indicate three anatomic parts including lumbar, sacral, and coccygeal vertebrae. The muscle of the tail base is indicated in flesh color and tendons across the caudal vertebra are indicated in gray. A magnified lateral view of Co2-Co8 is shown below.

(**B**) Oblique view of FEM of mouse vertebra. The curved arrow indicates the lateroflexion.

(**C**) The force (red arrow) and moment (blue arrow) of each disc are captured during the flexion. Dynamics of force and moment of each disc (colored lines) during the lateroflexion.

(**D**) View of von Mises stress distributed in AF of mouse tail discs during lateroflexion (left). Magnified view showing the stress distribution of Co4/5 disc. Bar charts show the stress of NP, AF, and EP at the end of lateroflexion.

(**E**) Principal component analysis based on stresses of NP, AF, and EP throughout the flexion across

1082 Co2/3 to Co7/8 discs. Ellipses showing two group sets of discs.

1083 (**F**) Schematic of tendon detachment on mouse tail spine. The tendons surrounding the Co5 were
1084 surgically severed at P0 and spine segment specimens were harvested at P30.

1085 (**G**) Percentages of two types of discs ranging from Co2/3 to Co7/8 levels. *P* values for the
1086 significance of differences in composition between normal control and detached group are
1087 determined by two-tailed Fisher's exact tests (N = 35 for normal mice with sham operation and N
1088 = 23 for mice with tendon detachment).

1089 (**H**) Histopathological scores of type A and type C discs from normal control and detachment. Data
1090 are mean ± S.E. *P* values are determined by two-tailed Student's t-tests.

1091

1092 **Figure 7. TRPV4-mediated mechanoadaptation affects the function of type C disc**

1093 (**A**) Expression of mechano-sensitive genes in each cell cluster. The significance of differences in
1094 gene expression between type A and type C discs is determined using two-tailed Student's t-test.
1095 Cell clusters with $P < 0.05$ are boxed in black.

1096 (**B**) Representative immunofluorescent staining of PIEZO1 and TRPV4 in type A and type C discs
1097 (top). Quantification of positive cells in the NP region and AF region (bottom). Scale bar, 100 μm.
1098 *P* values were calculated using Student's t-tests.

1099 (**C**) Representative SOFG staining and immunofluorescent staining of COL II show the changes in
1100 type C disc of Trpv4-ko mice. Dashed lines indicate the border between NP and AF. Scale bar, 100
1101 μm.

1102 (**D**) Comparisons of mechanical properties between WT and Trpv4-KO mice assessed by
1103 compression test (top) and 3-point bending test (bottom) on type C discs. *P* values for differences
1104 between groups were assessed via two-tailed Student's t-tests (N = 5 for each group).

1105 (**E**) Schematic of GSK1016790A (Trpv4 agonist) injection to mouse tail spine. The injection is
1106 performed weekly starting from P0 and coccygeal spine segments are harvested at P30.

1107 (**F**) Representative SOFG staining shows the morphology changes of NP in type A discs of mice
1108 injected with GSK1016790A. Scale bar, 100 μm.

1109 (**F**) Histological scores of type A discs from control and injection groups. Data are mean ± S.E. *P*
1110 values are determined by two-tailed Student's t-tests.

1111

Figure 1

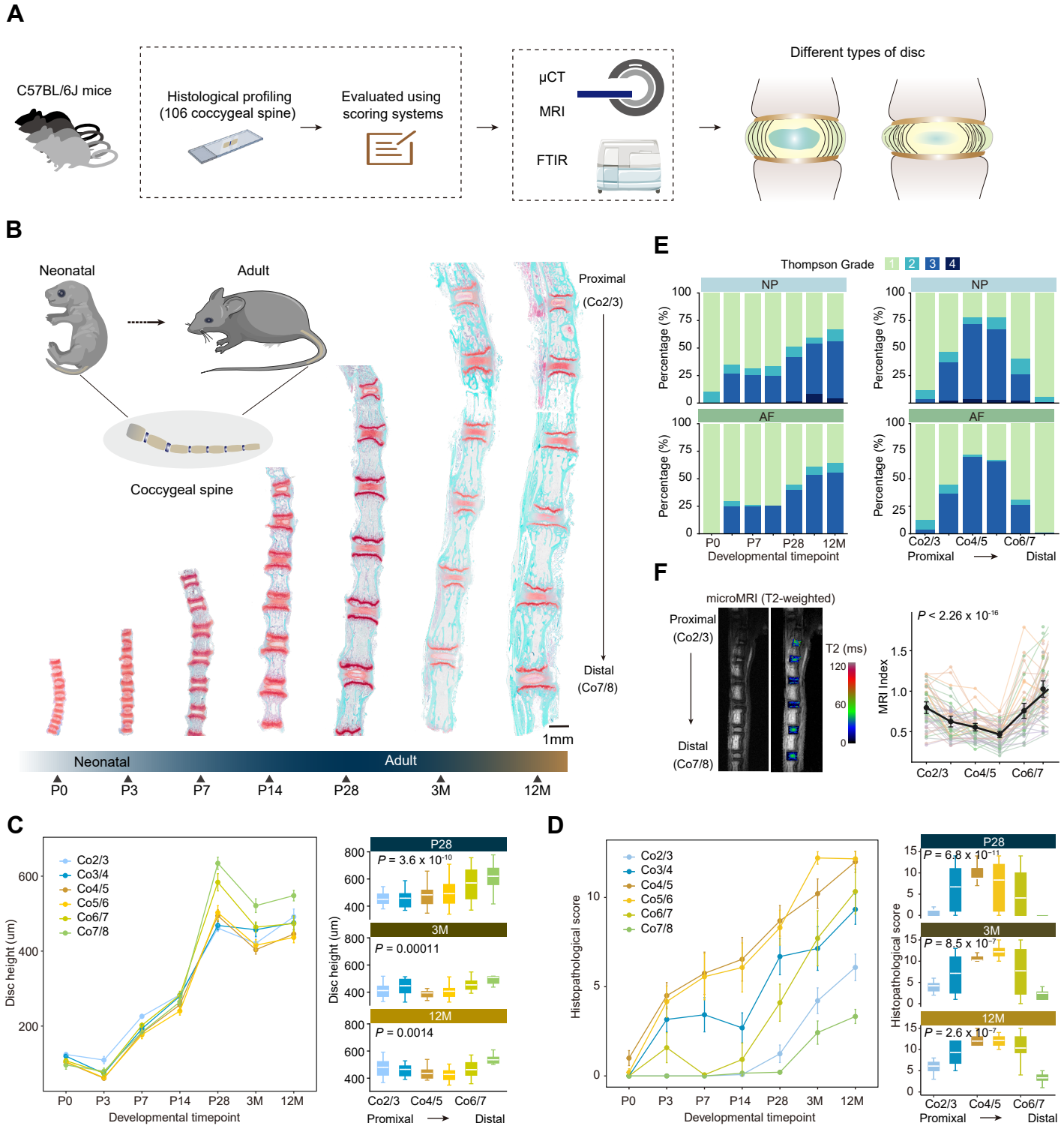
A
C57BL/6J mice
Histological profiling
(106 coccygeal spine)
Evaluated using
scoring systems
μCT
MRI
FTIR
Different types of disc
B
Neonatal
Adult
Coccygeal spine
Proximal
(Co2/3)
Distal
(Co7/8)
1mm
Neonatal
Adult
P0
P3
P7
P14
P28
3M
12M
E
Thompson Grade
1
2
3
4
NP
AF
Percentage (%)
Developmental timepoint
Co2/3
Co4/5
Co6/7
Promixal
Distal
F
microMRI (T2-weighted)
Proximal
(Co2/3)
Distal
(Co7/8)
T2 (ms)
MRI Index
P < 2.26 x 10-16
C
Co2/3
Co3/4
Co4/5
Co5/6
Co6/7
Co7/8
Disc height (um)
Developmental timepoint
P28
P = 3.6 x 10-10
3M
P = 0.00011
12M
P = 0.0014
D
Histopathological score
P28
P = 6.8 x 10-11
3M
P = 8.5 x 10-7
12M
P = 2.6 x 10-7

Figure 2

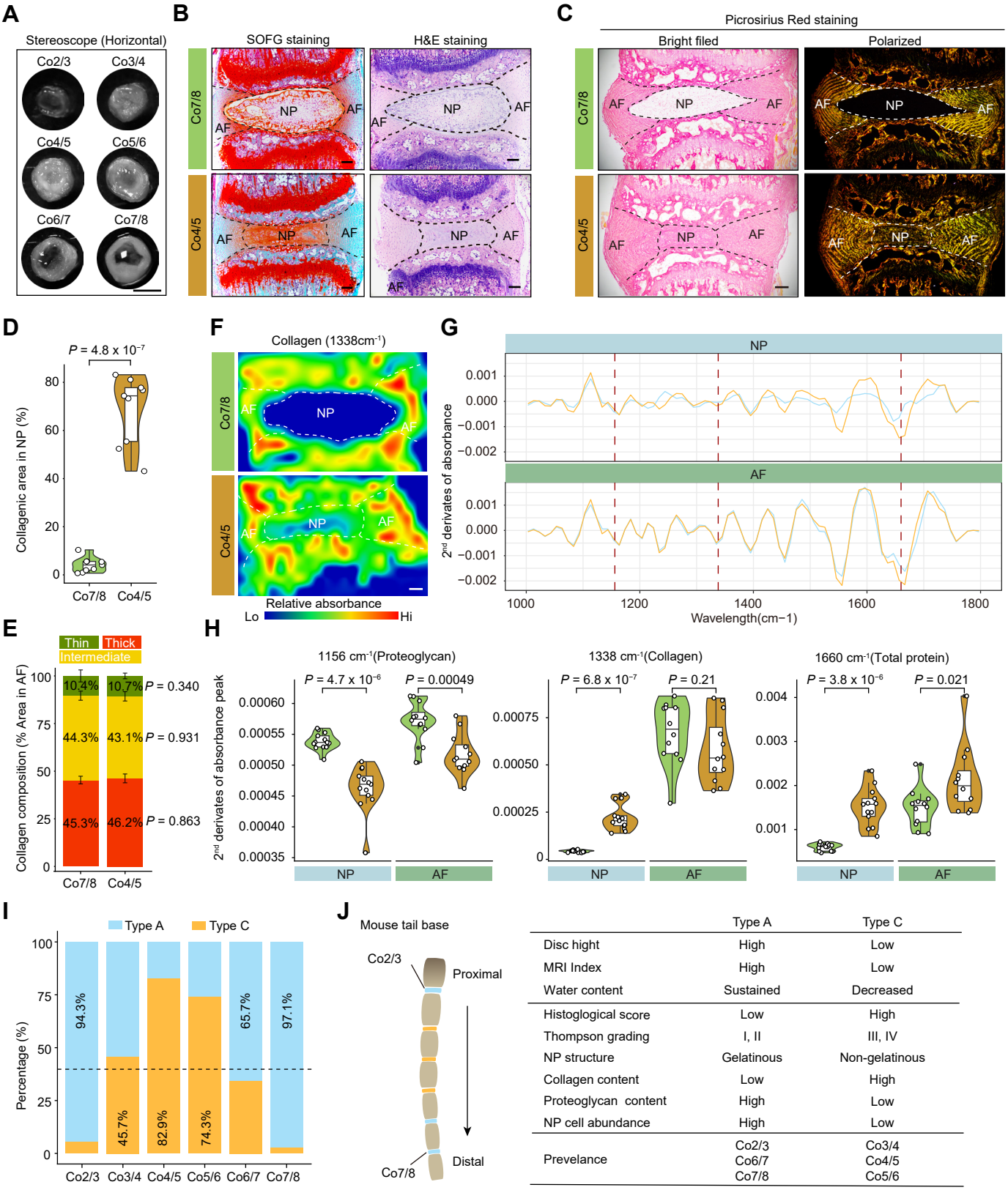

	Type A	Type C
Disc hight	High	Low
MRI Index	High	Low
Water content	Sustained	Decreased
Histoglogical score	Low	High
Thompson grading	I, II	III, IV
NP structure	Gelatinous	Non-gelatinous
Collagen content	Low	High
Proteoglycan content	High	Low
NP cell abundance	High	Low
Prevelance	Co2/3 Co6/7 Co7/8	Co3/4 Co4/5 Co5/6

Figure 3

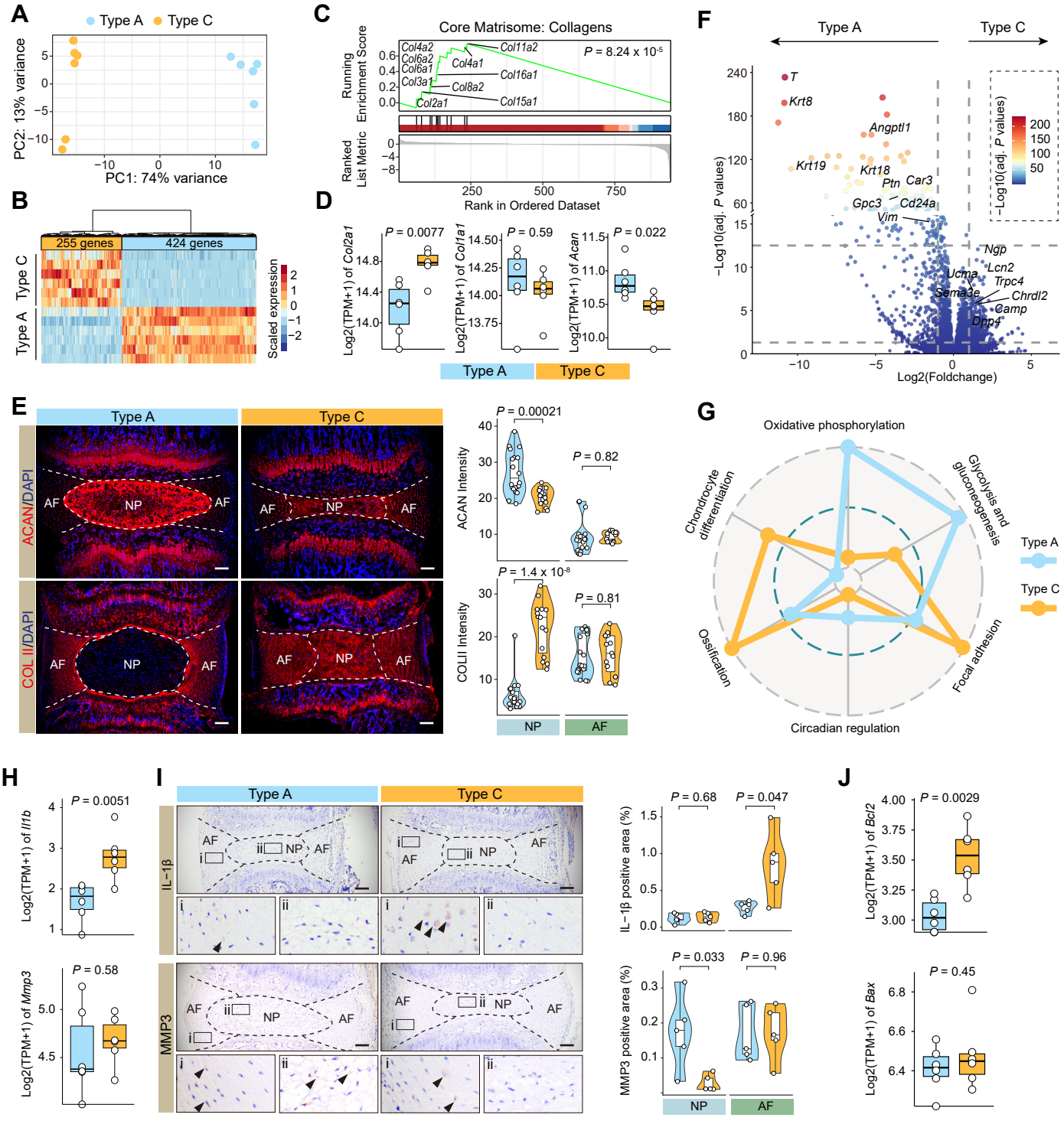
A
Type A
Type C
PC2: 13% variance
PC1: 74% variance
B
255 genes
424 genes
Type C
Type A
Scaled expression
C
Core Matrisome: Collagens
Running Enrichment Score
Ranked List Metric
Rank in Ordered Dataset
P = 8.24 x 10-5
Col4a2
Col6a2
Col6a1
Col3a1
Col2a1
Col11a2
Col4a1
Col16a1
Col8a2
Col15a1
D
P = 0.0077
P = 0.59
P = 0.022
Log2(TPM+1) of Col2a1
Log2(TPM+1) of Col1a1
Log2(TPM+1) of Acan
Type A
Type C
E
Type A
Type C
ACAN/DAPI
COL II/DAPI
AF
NP
P = 0.00021
P = 0.82
P = 1.4 x 10-8
P = 0.81
ACAN Intensity
COLII Intensity
NP
AF
F
Type A
Type C
−Log10(adj. P values)
Log2(Foldchange)
T
Krt8
Angptl1
Krt19
Krt18
Ptn
Car3
Gpc3
Cd24a
Vim
Ngp
Lcn2
Ucma
Trpc4
Sema3e
Chrdl2
Camp
Dpp4
G
Oxidative phosphorylation
Glycolysis and gluconeogenesis
Focal adhesion
Circadian regulation
Ossification
Chondrocyte differentiation
Type A
Type C
H
P = 0.0051
P = 0.58
Log2(TPM+1) of Il1b
Log2(TPM+1) of Mmp3
I
Type A
Type C
IL−1β
MMP3
AF
NP
i
ii
P = 0.68
P = 0.047
P = 0.033
P = 0.96
IL−1β positive area (%)
MMP3 positive area (%)
NP
AF
J
P = 0.0029
P = 0.45
Log2(TPM+1) of Bcl2
Log2(TPM+1) of Bax

Figure 4

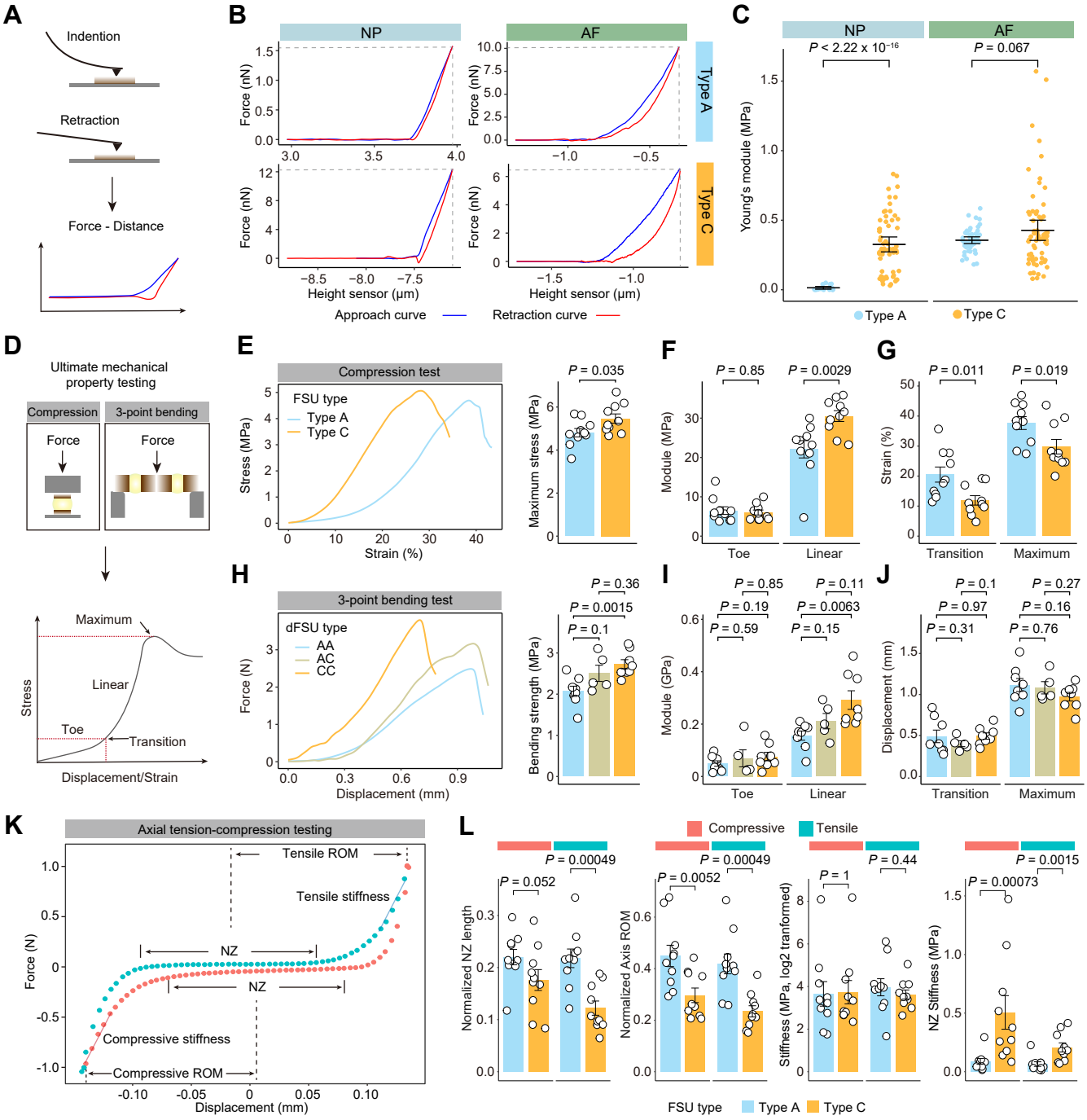
A
Indention
Retraction
Force - Distance
B
NP
AF
Type A
Type C
Force (nN)
Height sensor (μm)
Approach curve
Retraction curve
C
NP
AF
P < 2.22 x 10⁻¹⁶
P = 0.067
Young's module (MPa)
Type A
Type C
D
Ultimate mechanical property testing
Compression
3-point bending
Force
Maximum
Linear
Toe
Transition
Stress
Displacement/Strain
E
Compression test
FSU type
Type A
Type C
Stress (MPa)
Strain (%)
Maximum stress (MPa)
P = 0.035
F
P = 0.85
P = 0.0029
Module (MPa)
Toe
Linear
G
P = 0.011
P = 0.019
Strain (%)
Transition
Maximum
H
3-point bending test
dFSU type
AA
AC
CC
Force (N)
Displacement (mm)
Bending strength (MPa)
P = 0.36
P = 0.0015
P = 0.1
I
P = 0.85
P = 0.11
P = 0.19
P = 0.0063
P = 0.59
P = 0.15
Module (GPa)
Toe
Linear
J
P = 0.1
P = 0.27
P = 0.97
P = 0.16
P = 0.31
P = 0.76
Displacement (mm)
Transition
Maximum
K
Axial tension-compression testing
Tensile ROM
Tensile stiffness
NZ
NZ
Compressive stiffness
Compressive ROM
Force (N)
Displacement (mm)
L
Compressive
Tensile
P = 0.052
P = 0.00049
Normalized NZ length
P = 0.0052
P = 0.00049
Normalized Axis ROM
P = 1
P = 0.44
Stiffness (MPa, log2 tranformed)
P = 0.00073
P = 0.0015
NZ Stiffness (MPa)
FSU type
Type A
Type C

Figure 5

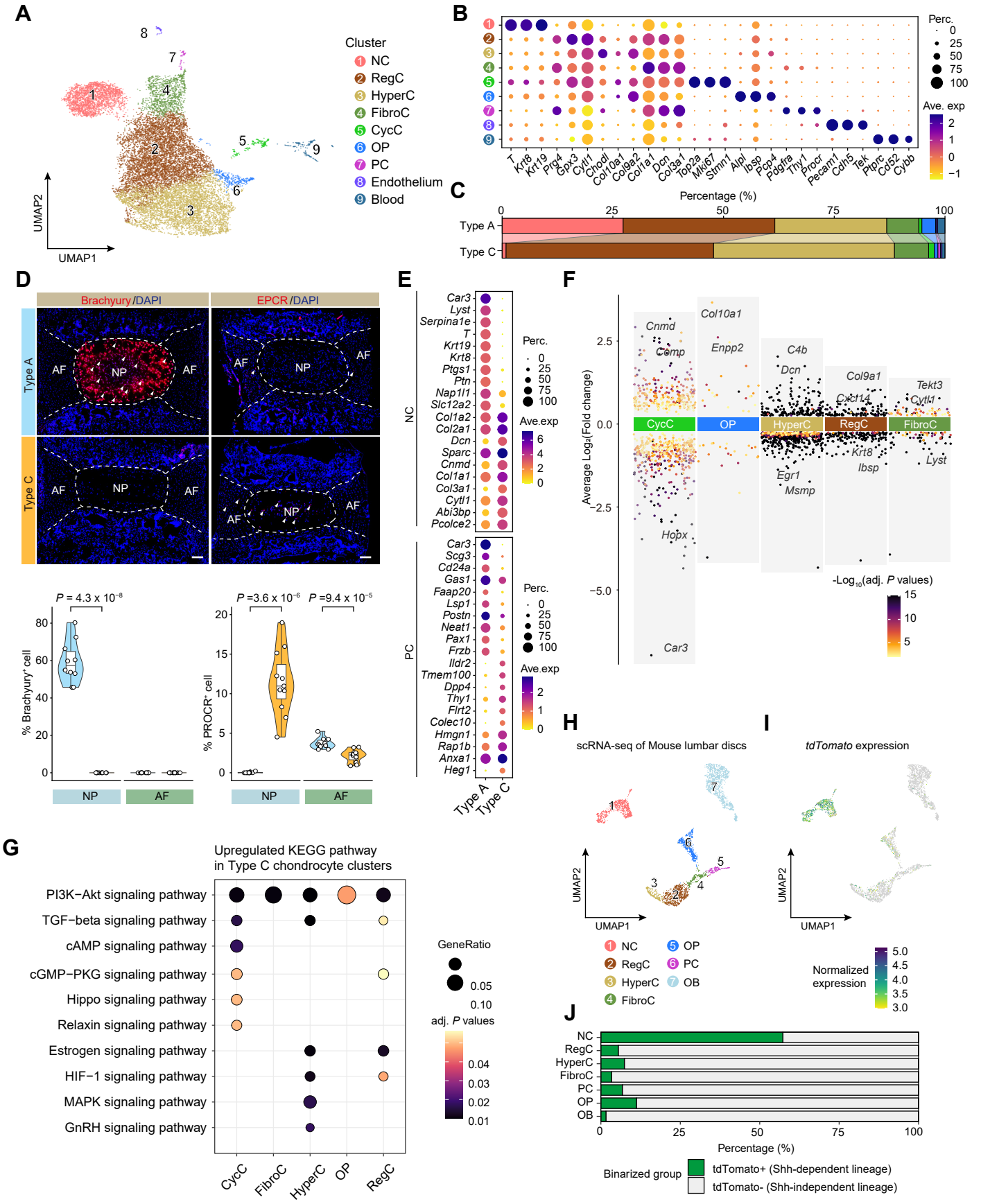
A
Cluster
1 NC
2 RegC
3 HyperC
4 FibroC
5 CycC
6 OP
7 PC
8 Endothelium
9 Blood
UMAP1
UMAP2
B
Perc.
Ave. exp
T
Krt8
Krt19
Prg4
Gpx3
Cytl1
Chodl
Col10a1
Col9a2
Col1a1
Dcn
Col3a1
Top2a
Mki67
Stmn1
Alol
Ibsp
Pcp4
Pdgfra
Thy1
Procr
Pecam1
Cdh5
Tek
Ptprc
Cd52
Cybb
C
Percentage (%)
Type A
Type C
D
Brachyury /DAPI
EPCR /DAPI
Type A
Type C
AF
NP
P = 4.3 x 10^-8
P =3.6 x 10^-6
P =9.4 x 10^-5
% Brachyury+ cell
% PROCR+ cell
NP
AF
E
NC
PC
Car3
Lyst
Serpina1e
T
Krt19
Krt8
Ptgs1
Ptn
Nap1l1
Slc12a2
Col1a2
Col2a1
Dcn
Sparc
Cnmd
Col1a1
Col3a1
Cytl1
Abi3bp
Pcolce2
Scg3
Cd24a
Gas1
Faap20
Lsp1
Postn
Neat1
Pax1
Frzb
Ildr2
Tmem100
Dpp4
Thy1
Flrt2
Colec10
Hmgn1
Rap1b
Anxa1
Heg1
Perc.
Ave.exp
Type A
Type C
F
Average Log2(Fold change)
Cnmd
Comp
Col10a1
Enpp2
C4b
Dcn
Col9a1
Cxcl14
Tekt3
Cytl1
CycC
OP
HyperC
RegC
FibroC
Hopx
Egr1
Msmp
Krt8
Ibsp
Lyst
Car3
-Log10(adj. P values)
G
Upregulated KEGG pathway
in Type C chondrocyte clusters
PI3K−Akt signaling pathway
TGF−beta signaling pathway
cAMP signaling pathway
cGMP−PKG signaling pathway
Hippo signaling pathway
Relaxin signaling pathway
Estrogen signaling pathway
HIF−1 signaling pathway
MAPK signaling pathway
GnRH signaling pathway
CycC
FibroC
HyperC
OP
RegC
GeneRatio
adj. P values
H
scRNA-seq of Mouse lumbar discs
UMAP1
UMAP2
1 NC
2 RegC
3 HyperC
4 FibroC
5 OP
6 PC
7 OB
I
tdTomato expression
Normalized expression
J
NC
RegC
HyperC
FibroC
PC
OP
OB
Percentage (%)
Binarized group
tdTomato+ (Shh-dependent lineage)
tdTomato- (Shh-independent lineage)

Figure 6

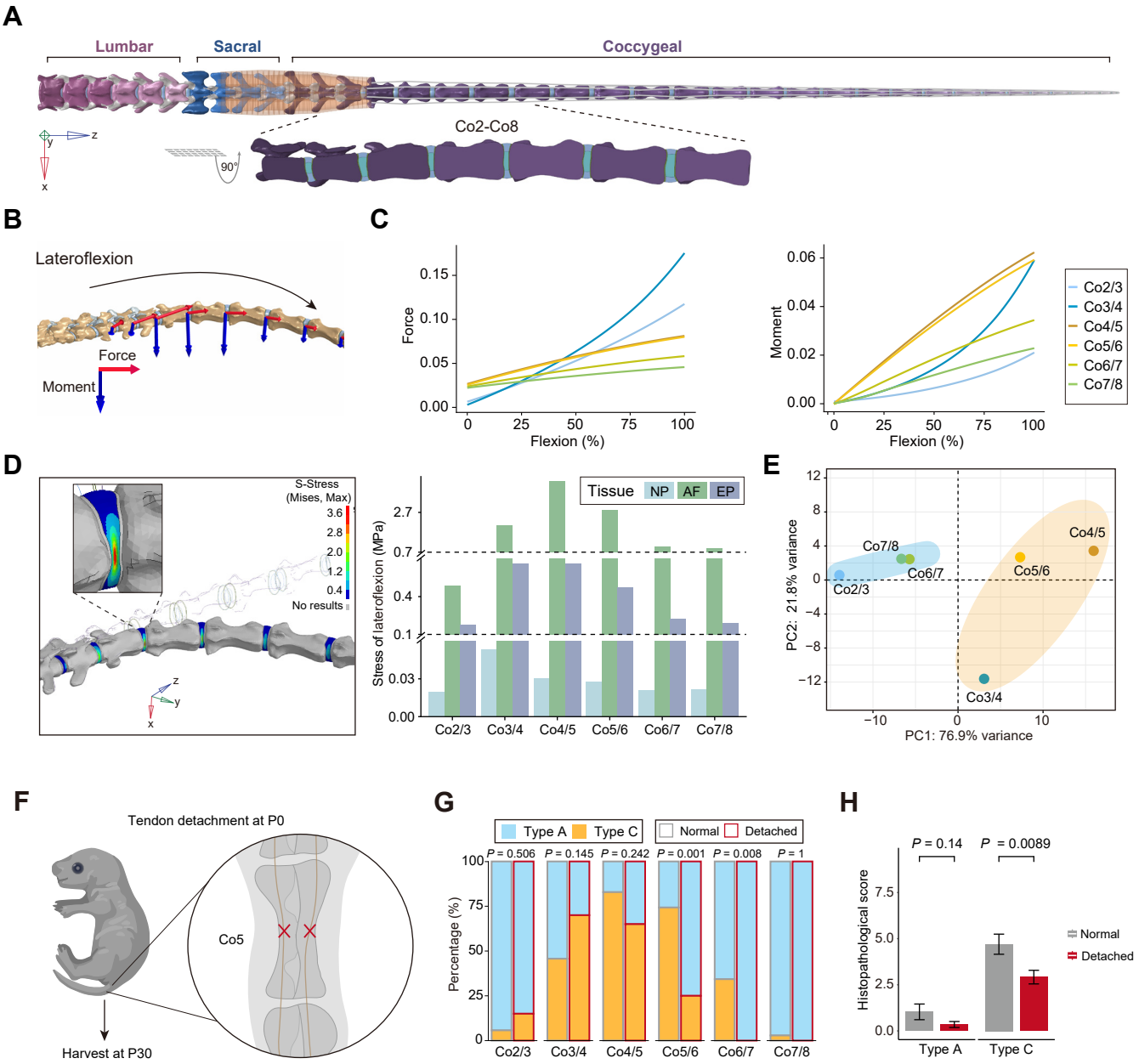
A
Lumbar
Sacral
Coccygeal
Co2-Co8
90°
B
Lateroflexion
Force
Moment
C
Force
Flexion (%)
Moment
Flexion (%)
Co2/3
Co3/4
Co4/5
Co5/6
Co6/7
Co7/8
D
S-Stress
(Mises, Max)
No results
Tissue
NP
AF
EP
Stress of lateroflexion (MPa)
E
PC2: 21.8% variance
PC1: 76.9% variance
F
Tendon detachment at P0
Co5
Harvest at P30
G
Type A
Type C
Normal
Detached
Percentage (%)
P = 0.506
P = 0.145
P = 0.242
P = 0.001
P = 0.008
P = 1
H
P = 0.14
P = 0.0089
Histopathological score
Type A
Type C

Figure 7

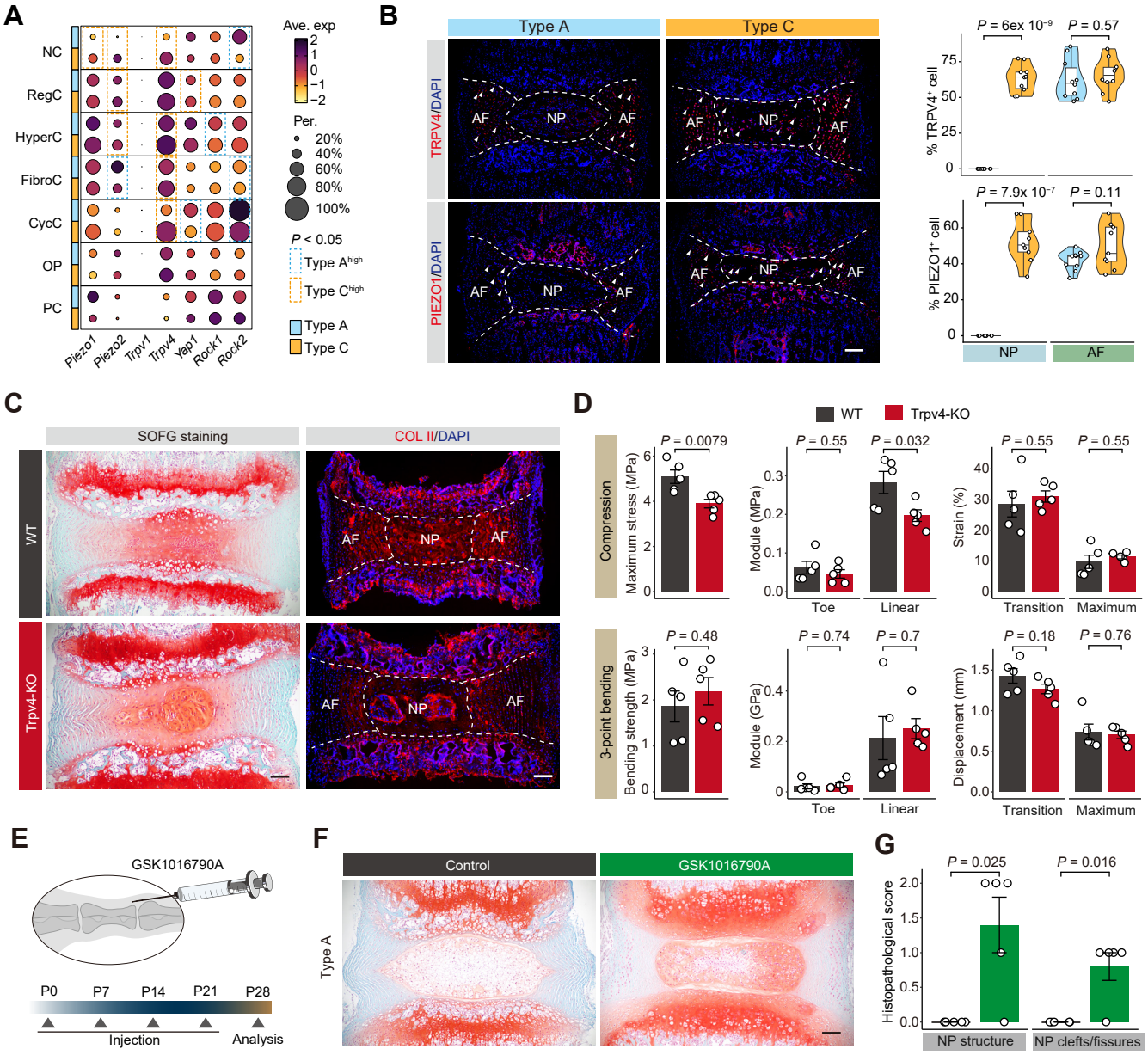
A
NC
RegC
HyperC
FibroC
CycC
OP
PC
Piezo1
Piezo2
Trpv1
Trpv4
Yap1
Rock1
Rock2
Ave. exp
Per.
20%
40%
60%
80%
100%
P < 0.05
Type A^high
Type C^high
Type A
Type C
B
Type A
Type C
TRPV4/DAPI
PIEZO1/DAPI
AF
NP
P = 6ex 10^-9
P = 0.57
% TRPV4+ cell
P = 7.9x 10^-7
P = 0.11
% PIEZO1+ cell
NP
AF
C
SOFG staining
COL II/DAPI
WT
Trpv4-KO
D
WT
Trpv4-KO
Compression
Maximum stress (MPa)
P = 0.0079
Module (MPa)
P = 0.55
P = 0.032
Toe
Linear
Strain (%)
P = 0.55
P = 0.55
Transition
Maximum
3-point bending
Bending strength (MPa)
P = 0.48
Module (GPa)
P = 0.74
P = 0.7
Toe
Linear
Displacement (mm)
P = 0.18
P = 0.76
Transition
Maximum
E
GSK1016790A
P0
P7
P14
P21
P28
Injection
Analysis
F
Control
GSK1016790A
Type A
G
Histopathological score
P = 0.025
P = 0.016
NP structure
NP clefts/fissures